

Bose Condensation and Lasing in Optical Microstructures

Part 2

Marzena Hanna Szymanska

Trinity College
University of Cambridge



Dissertation submitted for the degree
of Doctor of Philosophy at the
University of Cambridge

October 2001

Contents

I	Excitons in T-shaped quantum wires	1
1	Introduction	3
2	Calculations of the electron-hole states in T-shaped quantum wires	9
2.1	The model	10
2.1.1	Numerical method for calculating quantum wire exciton states . . .	11
2.1.2	Computational Method for Calculating the Single-Particle Wave Functions	12
2.1.3	Computational Method for Calculating the Matrix Elements	13
2.2	Results	15
2.2.1	Excited States	16
2.2.2	Trends in Confinement and Binding Energies	23
2.2.3	Optimisation of Confinement Energy for Experimental Realisation .	31
2.2.4	Accuracy of the Results	34
2.3	Conclusions	35
3	Two-mode Excitonic Lasing in T-shaped Quantum Wires	37
3.1	Experimental Set-up	37
3.2	Experimental Data	38
3.3	Calculations	41
3.4	Conclusions	42
4	Rate Equation Model for a Two-Mode Laser	47
4.1	Experimental Motivations	47
4.2	Model	48
4.3	Steady State Behaviour	51
4.4	Conclusion	56

5	Summary and Future Directions	59
5.1	Summary	59
5.2	Future Directions	60
A	Convergence of the T-shaped Wire Calculations	61
B	Comments on the Effective Mass Approximation	65
	Bibliography	68

Part I

Excitons in T-shaped quantum wires

Chapter 1

Introduction

Optical properties of electrons and holes confined to few dimensions are of interest for optical and electronic devices. As the dimensionality of the structure is reduced, the density of states tends to bunch together leading to a singularity in the 1D case. This effect can be very useful for low-threshold laser applications. At the same time the excitonic interaction in 1D is enhanced with respect to that in 3D and 2D structures. Quantum confinement leads to an increase in the exciton binding energy, E_b , and the oscillator strength for radiative recombination. Both effects provide possibilities for much better performance of optical devices such as semiconductor lasers.

The binding energy of a ground-state exciton in an ideal 2D quantum well is four times that in the 3D bulk semiconductor. For the ideal 1D quantum wire E_b diverges. This suggests that E_b for quasi-1D wires can be greatly increased with respect to the 2D limit for very thin wires with high potential barriers. 3D and 2D excitons dissociate at room temperature in GaAs to form an electron-hole plasma. To make them useful for real device applications, their binding energy needs to be increased and this might be achieved by using 1D quantum confinement.

Technologically it is very difficult to manufacture good quality 1D quantum wires with confinement in both spatial directions. They can be obtained from a 2D quantum well, fabricated by thin-film growth, by lateral structuring using lithographic methods. The accuracy of this method is, however, limited to some ten nanometers and thus the electronic properties of samples constructed in this way typically have a strong inhomogeneous broadening. Fortunately it appears possible to achieve quasi-1D particles even without a rigorous confinement in any of the spatial directions. This has been realised in so called V and T-shaped quantum wires. V-shaped quantum wires are obtained by self-organised

growth in pre-patterned materials such as chemically etched V-shaped grooves in GaAs substrates. The T-shaped quantum wire, first proposed by Chang et al. [1], forms at the intersection of two quantum wells and is obtained by the cleaved edge over-growth (CEO) method, a molecular-beam epitaxy (MBE) technique. The accuracy of this method is extremely high and allows fabrication of very thin (less than the Bohr radius of an exciton) wires with small thickness fluctuations. These structures are currently the subject of intensive research and have been realised by several groups [2]- [8].

Experimentalists try to optimise the geometry and the materials in order to increase the binding energy of the excitons, E_b , and the confinement energy, E_{con} for possible room temperature applications. Up until now, the most popular material studied experimentally has been GaAs/ $\text{Al}_x\text{Ga}_{1-x}\text{As}$. Increasing the Al molar fraction, x , should lead to bigger E_b and E_{con} but, unfortunately, for larger x the interfaces get rougher which degrades the transport properties. Thus optimised geometries for lower values of x become more relevant.

The confinement energy, E_{con} , is the energy difference between the lowest excitonic state in the wire and the lowest excitonic state in the 2D quantum well. It can be directly measured as the difference between the photoluminescence peaks obtained in a quantum wire (QWR) and a quantum well (QW). It is, however, not possible to measure the exciton binding energy directly. Its value has to be obtained from a combination of experimental data and one-particle calculations of electron and hole energies in a wire. There has been a disagreement between the purely theoretical values [10]- [14] and those obtained from a combination of experimental data and theoretical calculations. The confinement energies, however, tend to agree between experiment and purely theoretical calculations, suggesting that experiment, using combined methods where errors tend to accumulate, usually overestimates the binding energy.

For the 5-nm scale symmetric GaAs/AlAs, Someya et al. [3] reported the largest confinement energy for excitons in symmetric wires (Figure 1.1), $E_{con}=38$ meV and $E_b=27\pm 3$ meV. The largest confinement energy of any structure was reported by Gislason et al. [4,5] for their optimised wires. Using asymmetric wells with different widths and Al content as in Figure 1.2, they obtained an exciton confinement energy of 54 meV. Recently there has also been the first experimental realisation of T-shaped wires using $\text{In}_y\text{Ga}_{1-y}\text{As}/\text{Al}_{0.3}\text{Ga}_{0.7}\text{As}$ [2]. The highest confinement energy reported for this structure is 34 meV, which is very close to the GaAs/AlAs result, and the quality of the structure can be much higher than for the GaAs/AlAs case.

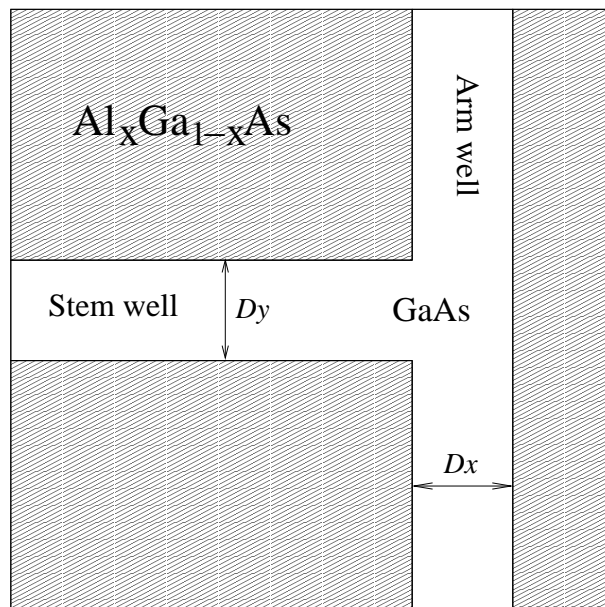


Figure 1.1: Shape of the symmetric T-shaped wire with notations.

Laser emission from the lowest exciton state in atomically smooth semiconductor quantum wires was first observed by Wegscheider et al. [6] in symmetric, T-shaped quantum wires made on the intersection of two 70 Å GaAs quantum wells surrounded by AlGaAs with the Al fraction $x = 0.35$. Recently the same group obtained excitonic lasing in a 60 Å/140 Å asymmetric quantum wire with a 7% Al filled Stem well (see Figure 1.2 [8]). They reported an interesting observation of two-mode lasing in this structure. Under strong excitation they achieved simultaneous lasing from two different states. There is a switching between those two lasing modes as the temperature or pumping rate is changed. A simple rate equation model (Chapter 4) gives very good agreement with experimental data, which suggests that we have lasing from two different excitonic states in the structure.

All calculations published to date which include the Coulomb interaction between the electron and hole have only examined the ground state exciton. They have used either variational methods [12]–[14] or other approximations [10,11] and were performed only for symmetric wires and for very limited cases realised experimentally in the early days of T-shaped wire manufacturing. With the growing experimental realisation of these structures as well as the interesting report of lasing phenomena there is a need for accurate two-body calculations, treating on an equal footing the single-particle potential and the Coulomb

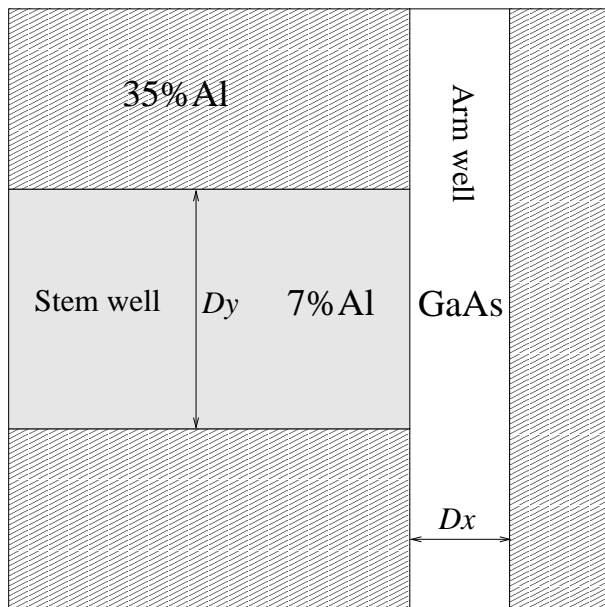


Figure 1.2: Shape of the asymmetric T-shaped wire with notations.

interaction, of both the ground and excited states in the structure.

Excited states seem to be very important for the operation of excitonic lasers [8]. Calculations of energies, oscillator strengths for radiative recombination (i.e, how the various states couple to photons) as well as the full wave functions for the whole spectra of interest would be very beneficial for understanding the origins of certain transitions and effects. This could help in the design of lasers with better properties and higher maximum temperatures for excitonic lasing. The goal is to design excitonic lasers which can operate at room temperature. Also, performing highly accurate calculations of the ground state exciton in QWR and the corresponding QW enables E_b and E_{con} to be obtained for different geometries (both symmetric and asymmetric) for a wide range of well widths and Al content, x . Such data are of great importance for the optimisation of the structures.

In Chapter 2 we present numerical calculations of electron-hole states in a T-shaped quantum wire. Our method is based on an exact numerical solution of the Schrödinger equation in a certain basis within the effective mass approximation. The method is not restricted to a given number of excited states and we can calculate as many of them as required. For some structures we have calculated up to 100 excited states. We perform calculations for a very wide range of T-shaped wires. In Section 2.1 the numerical method

is discussed in detail while in Section 2.2 we present the results. There we first study the spectra and wave functions and present a discussion of the nature of the various excited states. Finally we discuss E_{con} , E_b and the difference between the ground-state exciton energy and the first excited-state energy, E_{2-1} , as a function of well width Dx and Al molar fraction x for the symmetric and asymmetric quantum wires. Our calculations are being used to design improved excitonic lasers which will operate at room temperature.

In Chapter 3 we describe an experimental observation of two-mode lasing in a 60 Å/140 Å asymmetric quantum wire with a 7% Al filled Stem well [8]. This experiment, done at Bell-Laboratories, was a direct motivation for our work. We have performed the numerical calculations described in Chapter 2 for samples used in this experiment and have identified the origin of transitions which correspond to the two lasing modes.

In Chapter 4 we develop a rate equation model for a two-mode laser in which the two lasing modes come from two different excitonic states in the wire. This model gives very good agreement with the experimental data described in Chapter 3, which suggests that we have lasing from two different excitonic states in the quantum wire. The origin of this excitonic states can be determined from the detail numerical calculations presented for this experiment in Chapter 3.

Chapter 2

Calculations of the electron-hole states in T-shaped quantum wires

We calculate energies, oscillator strengths for radiative recombination, and two-particle wave functions for the ground state exciton and around 100 excited states in a T-shaped quantum wire. We include the single-particle potential and the Coulomb interaction between the electron and hole on an equal footing, and perform exact diagonalisation of the two-particle problem within a finite basis set. We calculate spectra for all of the experimentally studied cases of T-shaped wires including symmetric and asymmetric GaAs/Al_xGa_{1-x}As and In_yGa_{1-y}As/Al_xGa_{1-x}As structures. We study in detail the shape of the wave functions to gain insight into the nature of the various states for selected symmetric and asymmetric wires in which laser emission has been experimentally observed. We also calculate the binding energy of the ground state exciton and the confinement energy of the 1D quantum-wire-exciton state with respect to the 2D quantum-well exciton for a wide range of structures, varying the well width and the Al molar fraction x . We find that the largest binding energy of any wire constructed to date is 16.5 meV. We also notice that in asymmetric structures, the confinement energy is enhanced with respect to the symmetric forms with comparable parameters but the binding energy of the exciton is then lower than in the symmetric structures. For GaAs/Al_xGa_{1-x}As wires we obtain an upper limit for the binding energy of around 25 meV in a 10 Å wide GaAs/AlAs structure which suggests that other materials must be explored in order to achieve room temperature applications. There are some indications that In_yGa_{1-y}As/Al_xGa_{1-x}As might be a good candidate.

2.1 The model

We use the effective mass approximation with an anisotropic hole mass to describe an electron in a conduction band and a hole in a valence band in the semiconductor structures under consideration (see Appendix B). The effective mass of the hole depends on the crystallographic direction in the plane of the T-shaped structure. We consider the heavy hole only. The other bands (split off bands, light holes) would have energies higher than the region of interest for us. The light hole exciton, the closest in energy to the heavy hole exciton, is calculated to be over 30 meV higher than the heavy hole exciton, and thus it is ignored in the calculations. The electron and hole are in the external potential of the quantum wire formed at the T-shaped intersection of the GaAs/Al_xGa_{1-x}As quantum wells. The so called Arm quantum well is grown in the 110 crystal direction and intersects with a Stem quantum well grown in the 001 direction (see Figures 1.1 and 1.2). In our model the crystal directions 110, 001, and 110 correspond to x , y , and z respectively. We consider symmetric quantum wires where the Arm and Stem well are both of the same width, i.e, $Dx = Dy$, and are made of GaAs. We also consider asymmetric wires where the Stem well is significantly wider but filled with Al_xGa_{1-x}As with a low Al content to compensate for the reduction in confinement energy. Our method is applicable to any structure regardless of its shape and materials provided the external potential is independent of z

The value of the band-gap is different for the different materials used in the well construction. This gives rise to the potential barriers at the interfaces between the GaAs, Al_xGa_{1-x}As and InGaAs which take different values for electrons and holes. In our model the electron and hole are placed in external potentials $V_e(x, y)$ and $V_h(x, y)$, respectively, and interact via the Coulomb interaction. We choose the potential in GaAs to be zero and calculate all potentials in other materials with respect to this level. The external potential is independent of z in all cases. Sample geometries considered in this work are shown in Figs. 1.1 and 1.2. Using the above model, after the separation of the centre of mass and relative motion in the z direction, the system is described by the following Hamiltonian:

$$H = -\frac{\hbar^2}{2m_e} \nabla_{x_e, y_e}^2 - \frac{\hbar^2}{2m_{hx}} \nabla_{x_h}^2 - \frac{\hbar^2}{2m_{hy}} \nabla_{y_h}^2 - \frac{\hbar^2}{2\mu_z} \nabla_z^2 + V_e(x_e, y_e) + V_h(x_h, y_h) - \frac{e^2}{4\pi\epsilon_0\epsilon\sqrt{(x_e - x_h)^2 + (y_e - y_h)^2 + z^2}}, \quad (2.1)$$

where $z = z_e - z_h$ and $\frac{1}{\mu_z} = \frac{1}{m_e} + \frac{1}{m_{hz}}$. The wave function associated with the centre of

mass motion in the z direction is a plane wave and this coordinate can be omitted from the problem.

2.1.1 Numerical method for calculating quantum wire exciton states

We calculate the ground and excited states in the structures of interest by a direct diagonalisation method. Due to the complexity of the external potential with its limited symmetry and sharp edges, none of the standard basis sets seem appropriate. We use the following basis set:

$$\psi(x_e, y_e, x_h, y_h, z_e - z_h) = \sum_{i,j,k} c_{i,j,k} \sin\left(z \frac{k\pi}{L_z} - \frac{k\pi}{2}\right) \chi_i^e(x_e, y_e) \chi_j^h(x_h, y_h), \quad (2.2)$$

where $\chi_i^e(x_e, y_e)/\chi_j^h(x_h, y_h)$ are electron/hole single-particle wave functions for a T-shaped potential without the electron-hole Coulomb interaction. In the z direction we introduce hard wall boundary conditions and use a standing-wave basis set.

Our basis set does not obey the so called cusp condition [17] which is satisfied whenever two particles come together. The divergence in the potential energy when the electron and hole come together must be exactly cancelled by an opposite divergence in the kinetic energy. The exact wave function must therefore have a cusp when the electron and hole are coincident. Using a basis in which every basis function obeys the cusp condition would reduce the size of the basis set required. For an isotropic hole mass it would be very easy to satisfy the cusp condition by multiplying the basis functions by the factor $e^{-\Lambda\sqrt{(x_e-x_h)^2+(y_e-y_h)^2+z^2}}$ which is just the hydrogenic wave function. Unfortunately there is no analytical solution when we introduce the anisotropic hole mass. Thus we choose not to satisfy the cusp condition and therefore have to use a larger basis set.

The diagonalisation is performed using a NAG library routine. Convergence is usually achieved with a basis set containing 20 of each of the single-particle wave functions and 20 standing waves in the z direction. Thus $20 \times 20 \times 20 = 8000$ basis functions are needed which gives 20^6 matrix elements. Only one quarter of the total number needs to be calculated as interchanging k_1 and k_2 leaves the matrix element unchanged while interchanging i_1 and j_1 with i_2 and j_2 gives its complex conjugate. This still leaves a great many matrix elements to be calculated. Thus to make the calculations feasible the matrix elements need to be calculated very rapidly (See Section 2.1.3).

2.1.2 Computational Method for Calculating the Single-Particle Wave Functions

The one-particle (electron and hole) wave functions, $\chi_i^e(x_e, y_e)$ and $\chi_j^h(x_h, y_h)$ in a T-shaped external potential are calculated using the conjugate-gradient minimisation technique with pre-conditioning of the steepest descent vector. A detailed explanation of this method can be found in reference [16]. We specify the external potential on a 2D grid and use periodic boundary conditions in the x and y directions so that we are able to use Fast Fourier Transform (FFT) methods to calculate the kinetic energy in Fourier space while the potential energy matrix elements are calculated in real space. The fast calculation of the energy matrix elements is crucial as they have to be calculated many times during the conjugate-gradient minimisation. The FFT provides very fast switching between real and Fourier space and makes the algorithm much more efficient, but the use of periodic boundary conditions introduces the problem of inter-cell interactions in the case of two particle calculations. To avoid this problem we place the unit cell in the middle of another, larger unit cell of infinite potential (see Figure 2.1 and the Section 2.1.3).

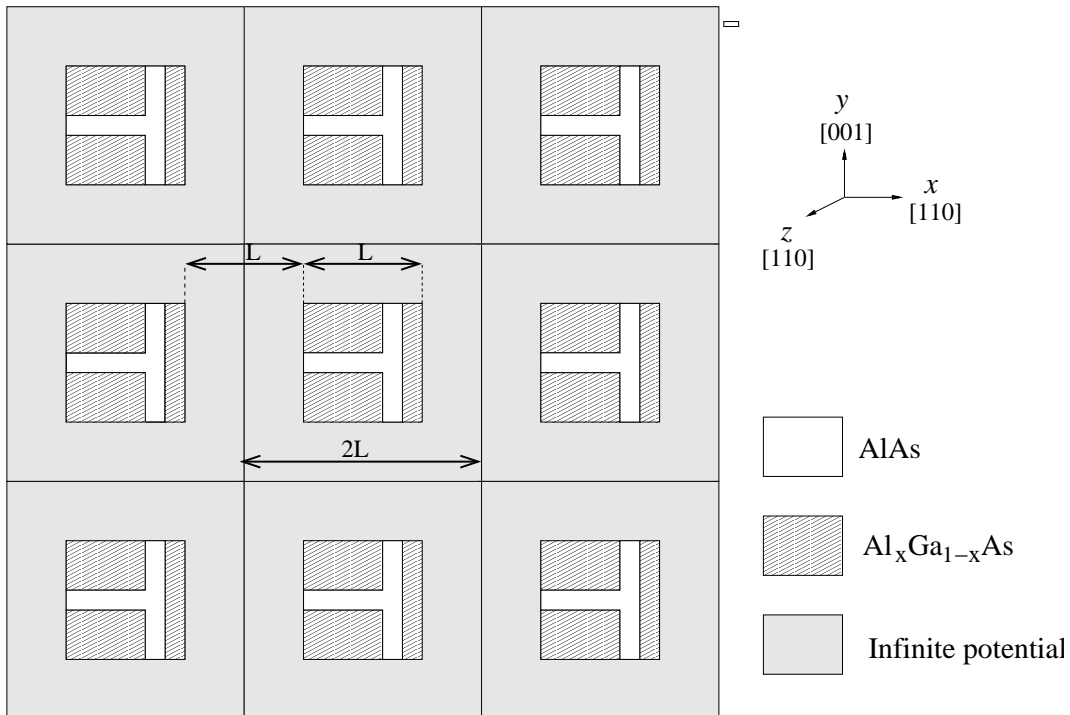


Figure 2.1: Lattice used for calculations and notations.

We use plane waves as a basis set for the one-particle problem. Using this method we can calculate as many as 50 states for the electron and 50 for the hole. Very good convergence with respect to the number of plane waves and the size of the unit cell is obtained (see Section 2.2.4).

2.1.3 Computational Method for Calculating the Matrix Elements

The kinetic and potential energies are diagonal in this basis and are obtained from the one-particle calculations. Thus only the Coulomb matrix elements need to be calculated.

A Coulomb matrix element in the basis set (2.2) is a 5D integral of the following form:

$$- \int \int \int \int \int dx_e dy_e dx_h dy_h dz \sin\left(z \frac{k_2 \pi}{L_z} - \frac{k_2 \pi}{2}\right) \chi_{i_2}^{e*}(x_e, y_e) \chi_{j_2}^{h*}(x_h, y_h) q(x_e - x_h, y_e - y_h, z) \sin\left(z \frac{k_1 \pi}{L_z} - \frac{k_1 \pi}{2}\right) \chi_{i_1}^e(x_e, y_e) \chi_{j_1}^h(x_h, y_h). \quad (2.3)$$

Where $q(x_e - x_h, y_e - y_h, z)$ is the Coulomb interaction cut off at final distance to avoid image effects (see below). This integral must be calculated numerically. Numerical integration for so many dimensions is very slow and thus is not feasible for the case of 20^6 matrix elements. Thus another method has to be introduced.

The above integral is of the form

$$- \int \int \int \int \int dx_e dy_e dx_h dy_h dz f_e(x_e, y_e) f_h(x_h, y_h) q(x_e - x_h, y_e - y_h, z) f_z(z). \quad (2.4)$$

Where

$$\begin{aligned} f_e(x_e, y_e) &= \chi_{i_2}^{e*}(x_e, y_e) \chi_{i_1}^e(x_e, y_e), \\ f_h(x_h, y_h) &= \chi_{i_2}^{h*}(x_h, y_h) \chi_{i_1}^h(x_h, y_h), \end{aligned} \quad (2.5)$$

Using the Fourier transform and the convolution theorem it can be shown that the above integral is equal to:

$$\int dz \sum_{G_x, G_y} F_e(-G_x, -G_y) * F_h(G_x, G_y) * Q(G_x, G_y, z). \quad (2.6)$$

Where F_e, F_h, Q are the 2D Fourier transforms of the function f_e with respect to x_e and y_e, f_h with respect to x_h and y_h and q with respect to $x_e - x_h$ and $y_e - y_h$, respectively. Thus the 5D integral can be reduced to a 1D integral with respect to the z variable and a 2D sum in Fourier space. The F_e and F_h Fourier transforms can be easily calculated using FFTs in real space after multiplication of the corresponding $\chi_{i_1}^e(x_e, y_e)$ by $\chi_{i_2}^{e*}(x_e, y_e)$ for electrons and $\chi_{i_1}^h(x_h, y_h)$ by $\chi_{i_2}^{h*}(x_h, y_h)$.

In order to use FFTs we need to introduce periodic boundary conditions in the x and y directions as in the one-particle calculations. To eliminate interactions between particles in neighbouring cells, we place the unit cell in the middle of another, bigger unit cell of infinite potential (see Figure 2.1).

The distance between the edges of successive small unit cells is exactly the width of the small unit cell, L . We cut-off the Coulomb interaction at a distance corresponding to the size of the small unit cell. We therefor consider the following form of Coulomb interaction:

$$q(x_e - x_h, y_e - y_h, z) = \begin{cases} -\frac{e^2}{4\pi\epsilon_0\epsilon\sqrt{(x_e-x_h)^2+(y_e-y_h)^2+z^2}} & \text{if } x_e - x_h < L_x \\ & \text{and } y_e - y_h < L_y \\ 0 & \text{otherwise.} \end{cases} \quad (2.7)$$

Particles interact only when their separations in the x and y directions are smaller than L_x and L_y respectively. The separations of particles in neighbouring cells is always bigger than the cut-off and thus they do not interact. Particles in the same unit cell are always separated by less than that the cut-off distance due to the infinite potential outside the small unit cell. Thus we take into account all of the physical Coulomb interaction and completely eliminate the interactions between images. In the numerical implementation the infinite potential is replaced by a large but finite potential. Thus the probability of the particle being outside the small unit cell is effectively zero and we find that the results do not depend on the value of this potential for values greater than around three times the potential in the $\text{Al}_x\text{Ga}_{1-x}\text{As}$ region.

The 2D Fourier transform of the 3D Coulomb interaction with a cut-off cannot be done analytically. Thus we put the Coulomb interaction onto a 2D grid as a function of relative coordinates $x_e - x_h$ and $y_e - y_h$ for every z value. The unit cell in relative coordinates will go from $-L_x$ to L_x , and $-L_y$ to L_y respectively. Then for every value of z a 2D FFT is performed with respect to $x_e - x_h$ and $y_e - y_h$ and the results stored in the 3D array $Q(G_x, G_y, z)$. Since this is the same for every matrix element the above calculation needs to be performed only once.

The calculations described by eqn. (2.6) need to be performed for every matrix element. After $F_e(G_x, G_y)$ and $F_h(G_x, G_y)$ have been calculated the summation over the reciprocal lattice vectors G_x and G_y for every value of z is performed. The remaining 1D integral in the z direction is done numerically, after interpolation of data points, using a routine from the NAG library. The dependence of the integrand on z is found to be very smooth and thus not many points are required to obtain accurate results.

2.2 Results

We perform the calculations for a series of T-shaped structures. We calculate energies, oscillator strengths and wave functions for the first 20-100 two-particle states for symmetric and asymmetric wires.

For symmetric wires we consider the structure denoted by W which has been experimentally studied by Wegscheider et al. [6] and consists of GaAs/Al_{0.35}Ga_{0.65}As 70 Å quantum wells. Then, keeping the rest of parameters constant, we vary the quantum well width from 10 Å to 80 Å in steps of 10 Å in order to examine the width dependence of the various properties. We also perform calculations for samples denoted by S1 and S2 studied by Someya et al. [3] made of GaAs/Al_{0.3}Ga_{0.7}As (S1) and GaAs/AlAs (S2) quantum wells of width around 50 Å. For the GaAs/AlAs case we again vary the well width from 10 Å to 60 Å. Then we take an intermediate value of the Al molar fraction, $x = 0.56$, and vary the well width from 10 Å to 60 Å in order to examine the dependence on the well width as well as Al content. Finally we perform calculations for 35 Å-scale In_{0.17}Ga_{0.83}As/Al_{0.3}Ga_{0.7}As (denoted by N4) as well as for 40 Å-scale In_{0.09}Ga_{0.91}As/Al_{0.3}Ga_{0.7}As (denoted by N2) samples as studied experimentally by Akiyama et al. [2].

For asymmetric structures we consider the wire studied experimentally by Rubio et al. [8] which consists of a 60 Å GaAs/Al_{0.35}Ga_{0.65}As Arm quantum well and a 140 Å Al_{0.07}Ga_{0.93}As/Al_{0.35}Ga_{0.65}As Stem quantum well. We vary the width of the Arm quantum well from 50 Å to 100 Å. We also perform calculations for the asymmetric structure studied by a different group [4, 5] which consists of a 25 Å GaAs/Al_{0.3}Ga_{0.7}As Arm quantum well and a 120 Å Al_{0.14}Ga_{0.86}As/Al_{0.3}Ga_{0.7}As Stem quantum well.

In the first part of this section we present the spectra for symmetric and asymmetric quantum wires with the positions of 2D exciton, 1D continuum (unbound electron and hole both in the wire) and 1De/2Dh continuum (unbound electron in the wire and hole in the well) states as well as pictures of representative wave functions. This allows us to discuss

the nature of the excited states in the structures. In the second part we discuss the trends in confinement and binding energy and the separation in energy between the ground and the first excited states as a function of the well width and Al fraction.

We use a static dielectric constant $\epsilon=13.2$ and a conduction band offset ratio $Q_c = \Delta E_{cond}/\Delta E_g$ of 0.65. For the difference in bandgaps on the GaAs/Al_xGa_{1-x}As interface we use the following formula: $\Delta E_g = 1247 \times x$ meV for $x < 0.45$ and $1247 \times x + 1147 \times (x - 0.45)^2$ meV for $x > 0.45$. For the electron mass we use $m_e = 0.067m_0$ while for the hole mass $m_{hx} = m_{hz} = m_{h[110]} = 0.69 - 0.71m_0$ and $m_{hy} = m_{h[001]} = 0.38m_0$ (m_0 is the electron rest mass). For the In_{0.09}Ga_{0.91}As/Al_{0.3}Ga_{0.7}As (In_{0.17}Ga_{0.83}As/Al_{0.3}Ga_{0.7}As) we use parameters from reference [2]: for the electron $m_e = 0.0647(0.0626)m_0$, for the hole $m_{hy} = m_{hh[001]} = 0.367(0.358)m_0$ and $m_{hx} = m_{hz} = m_{h[110]} = 0.682(0.656)m_0$, $\Delta E_g=464(557)$ meV and the band offset was assumed to be 65% in the conduction and 35% in the valence band.

2.2.1 Excited States

Symmetric Wires

In Figure 2.2 we show spectra (the oscillator strength versus energy) for the first 20 (30 in the case of the 70 Å and 30 Å wire) states for the GaAs/Al_{0.35}Ga_{0.65}As structure for well widths from 10 Å to 80 Å. A dashed line shows the energy of the 1D continuum, a dotted line that of the 1D electron and 2D hole continuum, the dotted-dashed line - the quantum-well 2D exciton, while the dashed-dot-dotted line shows the 2D electron and 2D hole continuum. In the case of the 20 Å wire the 2D electron and 2D hole continuum is not shown as its value of 245.5 meV is out of range by a significant amount. Because our system is finite in the z direction, we obtain only a sampling of the continuum states; below the continuum edge the states are discrete.

Note that for the experimentally studied 70 Å structure, the 2D exciton has a lower energy than the completely unbound electron and hole in the wire. The situation clearly depends on the well width and the crossing point is between 60 and 70 Å. For well widths of 60 Å or smaller, the 1D continuum (1Dcon) is lower in energy than the 2D exciton (2Dexc) with the difference being maximal for a width of around 20 Å. For widths of 70 Å or bigger, the 1Dcon is higher in energy than the 2Dexc with the difference growing for increasing well width. This effect might be significant for pumping T-shaped-wire lasers. Free electrons and holes are excited in the whole area of both wells and thus, when the

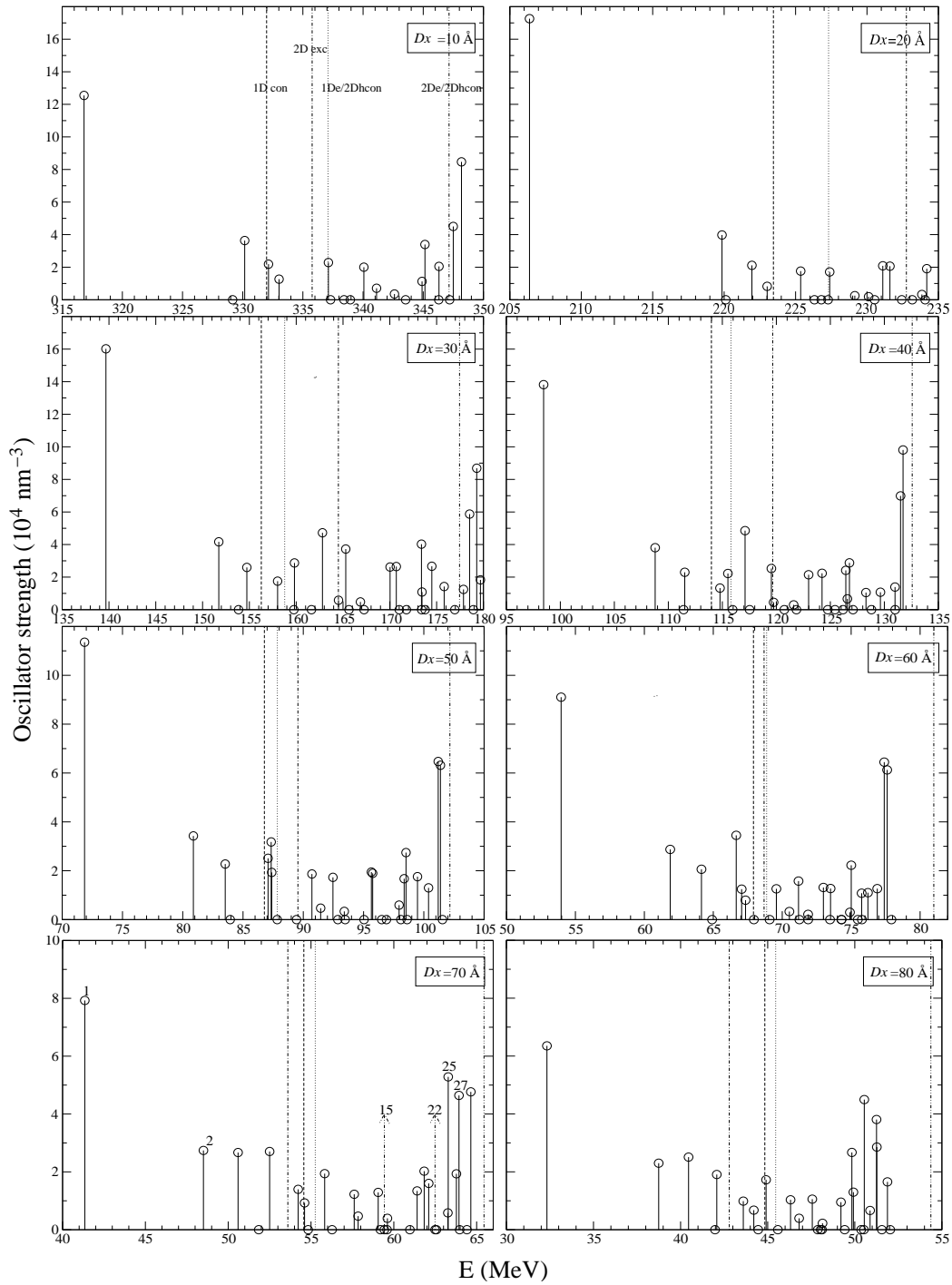


Figure 2.2: Oscillator strength versus energy for the lowest 20-30 states in a symmetric T-shaped structure for different well widths D_x .

2D exciton has a lower energy than the 1D continuum, formation of the 2D excitons is energetically favourable. These excitons can recombine in a well instead of going to the wire and forming a 1D exciton. Clearly it is more efficient to have the 1D continuum lower in energy than the 2D exciton.

By increasing the well width we obtain more states that are lower in energy than the 1Dcon and 2Dexc beginning with two (ground and the first excited) for the 10 Å well, three for widths between 20-50 Å and four states for larger widths.

We now discuss the behaviour of $|\psi|^2$ for the 70 Å case. The wave functions depend on five spatial coordinates and thus various cuts in 5D space are presented in Figures 2.3 and 2.4: a) the electron x_e, y_e position after averaging over the hole position, b) the hole x_h, y_h position after averaging over the electron position, and relative coordinates after averaging over the centre of mass position c) the $x_e - x_h, y_e - y_h$ relative coordinates for $z_e - z_h = 0$ and d) the $x_e - x_h, z$ relative coordinates for $y_e - y_h = 0$.

For the ground state we observe that the electron and hole are very well localised in the wire with slightly more hole localisation. The relative coordinate plots clearly show the bound exciton (Figure 2.3(1)).

The electron in the first excited state is localised in the wire while the hole already expands into the Arm well. The relative coordinate pictures show that the electron and hole are bound and form an exciton with an asymmetric shape. The size of the exciton is smallest in the x direction (the Stem well direction) and the exciton expands more into the y (the Arm well where the hole is expanded) and free z directions (Figure 2.3 (2)). The oscillator strength of this state is about 1/3 of that of the ground state and the state clearly takes the form of a 1D exciton with its centre of mass in the T-wire.

It can be seen from the spectra (Figure 2.2) that there are four states (apart from the ground state) with energies smaller than 1Dcon and 2Dexc. The nature of the 3rd and 5th states is very similar to the 2nd one: the centre of mass is in the wire and the electron is still well localised in the wire while the hole spreads into the wells (into both the Arm and Stem wells for the 3rd state while only into the Stem well for the 5th one). The relative coordinates show the complex, asymmetric shape of this excitonic state and the oscillator strength is again around 1/3 of the ground state exciton.

The 4th state with almost zero oscillator strength corresponds to a 1D continuum. The electron and hole are both in the wire but the relative coordinate pictures show an unbound exciton. Within the first 30 states we have 3 states of that nature: the 4th, 7th and 15th. The 15th state is shown in Figure 2.3: the electron and hole are confined in the wire (a,

b) and there are 3 nodes in the z direction and 1 node in the y direction. The other two states look similar and differ only in the number of nodes. The energy of the 4th state, which is the lowest 1Dcon state, turns out to be lower than the real 1Dcon obtained from our one-particle calculations. This is due to the finite size effects. Our method is very well converged with respect to the cell size for the bound state and for the unbound ones where at least one of the particles is in the well. However, for the unbound continuum 1D states, the particles are very close in the x, y plane because of the very small size of the wire and thus the interaction is stronger. Consequently it does not decay as fast in the z direction as other states and thus we need a much bigger unit cell in the z direction to achieve convergence. There are however only three such states within the 30 we examine and we know their true energies from the preceding one particle calculations.

For further excited states up to the 25th, the electron, and thus the centre of mass, is still localised in the wire while the hole is taking up more and more energetic states in both wells, where energies are quantised due to the finite size of the cell. Those states can be divided into two groups depending on their relative coordinate nature: excitonic-like states similar to the second state (Figure 2.3 (2)) and ionised states like the 22nd which is represented in Figure 2.4 (22). The oscillator strength of the second group is zero (see Figure 2.2).

The 25th state (Figure 2.4 (25)) is the first state where the electron is de-localised in both wells, the relative coordinates and the large oscillator strength shows that it is clearly an excitonic-like state. It appears to be a 2D quantum well exciton state scattered on the T shaped intersection. Its energy is thus higher than that of a pure 2Dexc.

The 27th state is the 2D Arm-quantum-well-exciton state. It has higher energy than the ground-state 2D exciton because the electron and hole wave functions occupy higher energy states than the ground state of the well due to the presence of the T intersection.

The 30th state has a very similar nature to the 27th but the exciton expands into the Stem instead of the Arm quantum well.

The 25th, 27th and 30th states all have large oscillator strengths (around 3/4 of that of the ground state exciton). It is interesting to note that between the ground state and those 2D large-oscillator-strength states, there is a group of states with relatively low oscillator strengths. The reason for this is that after the ground state, there are states where either the wire-like electron is bound to the well-like hole and thus they do not overlap enough to give big contribution to the spectrum or they consist of a wire like electron with an unbound hole.

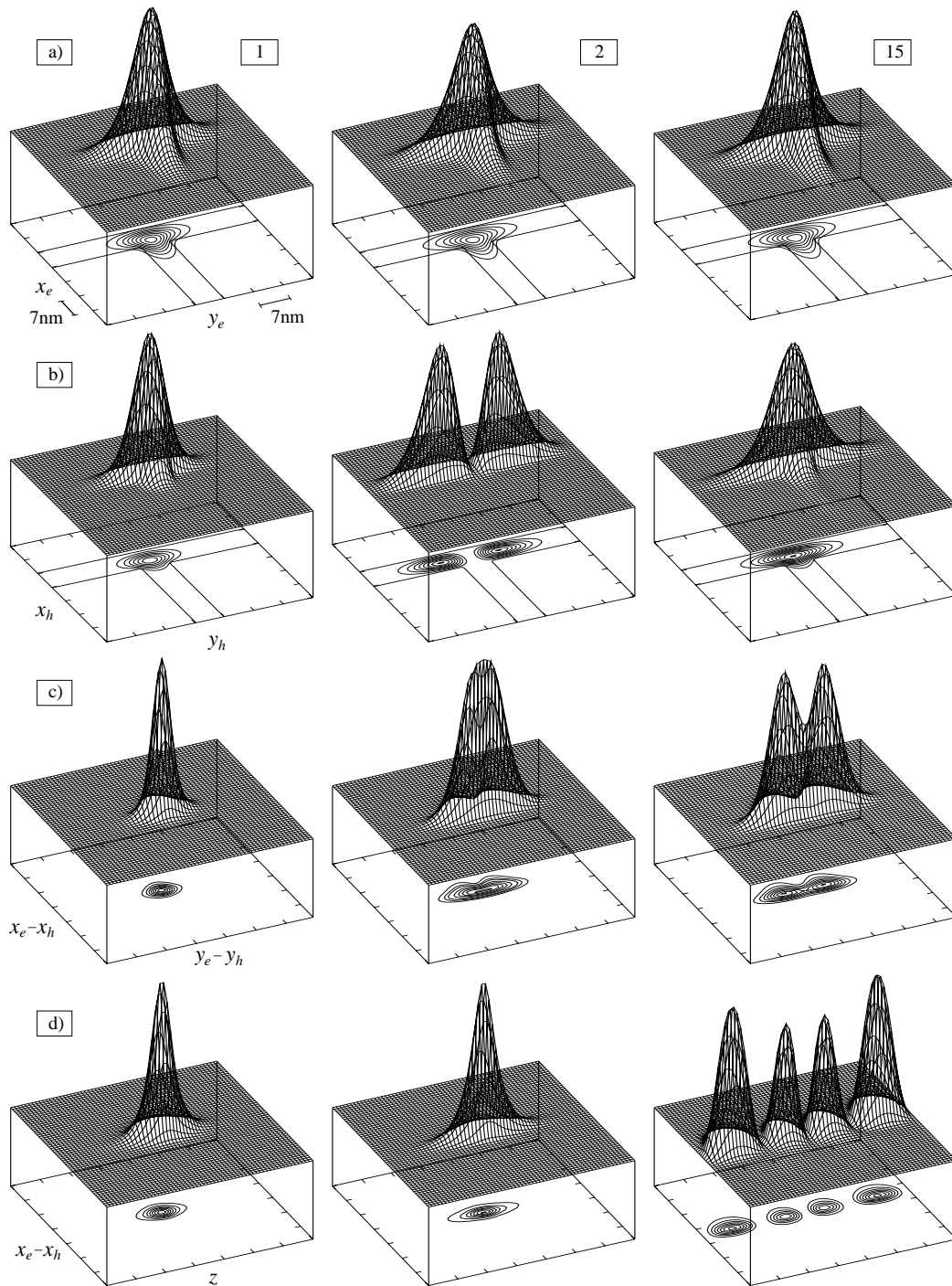


Figure 2.3: Modulus squared of the two-particle wave function for the ground (1), first excited (2) and the 15th (15) state in the symmetric T-structure. Electron (a), hole (b) and the relative coordinates $x_e - x_h$, $y_e - y_h$ (c), $x_e - x_h$, z (d) probability densities are shown.

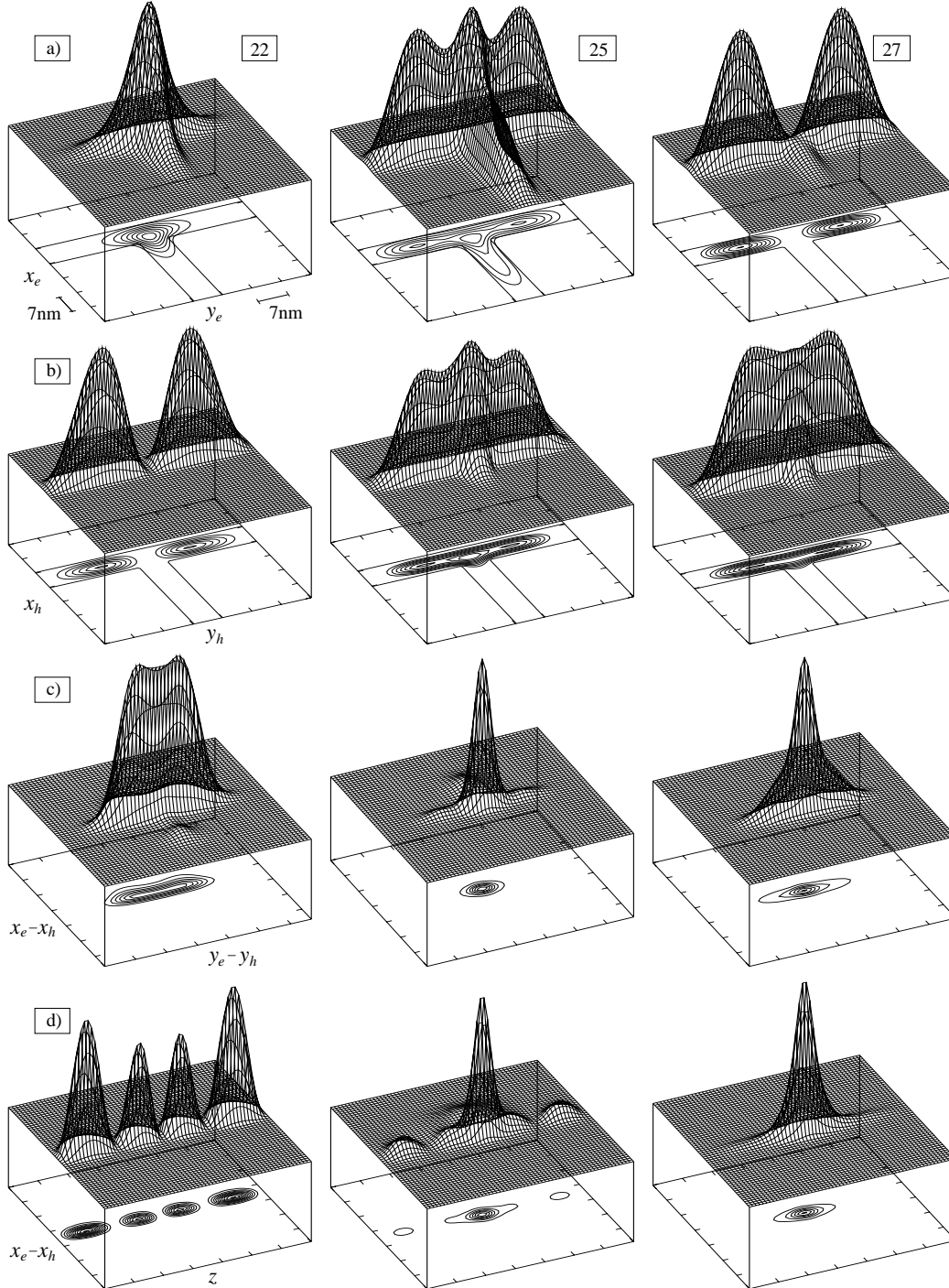


Figure 2.4: Modulus squared of the two-particle wave function for the 22th, 25th and the 27th state in the symmetric T-structure. Electron (a), hole (b) and the relative coordinates $x_e - x_h$, $y_e - y_h$ (c), $x_e - x_h$, z (d) probability densities are shown.

Those quantum-well-like exciton states that scattered on the T-shaped potential (like state 25) appear to be quite important for the excitonic lasing because of their big oscillator strength. In [8] the authors reported two-mode lasing in an asymmetric wire where the laser switches between the ground-state exciton and the other state whose energy corresponds to the state from the tail of the above mentioned states.

Asymmetric Wires

The asymmetric wire that we study in detail consists of a 60 Å or 56 Å GaAs/Al_{0.35}Ga_{0.65}As Arm quantum well and a 140 Å Al_{0.07}Ga_{0.93}As/Al_{0.35}Ga_{0.65}As Stem quantum well [8]. The spectrum for the 60 Å Arm case is shown in Figure 2.5. The nature of the states is very

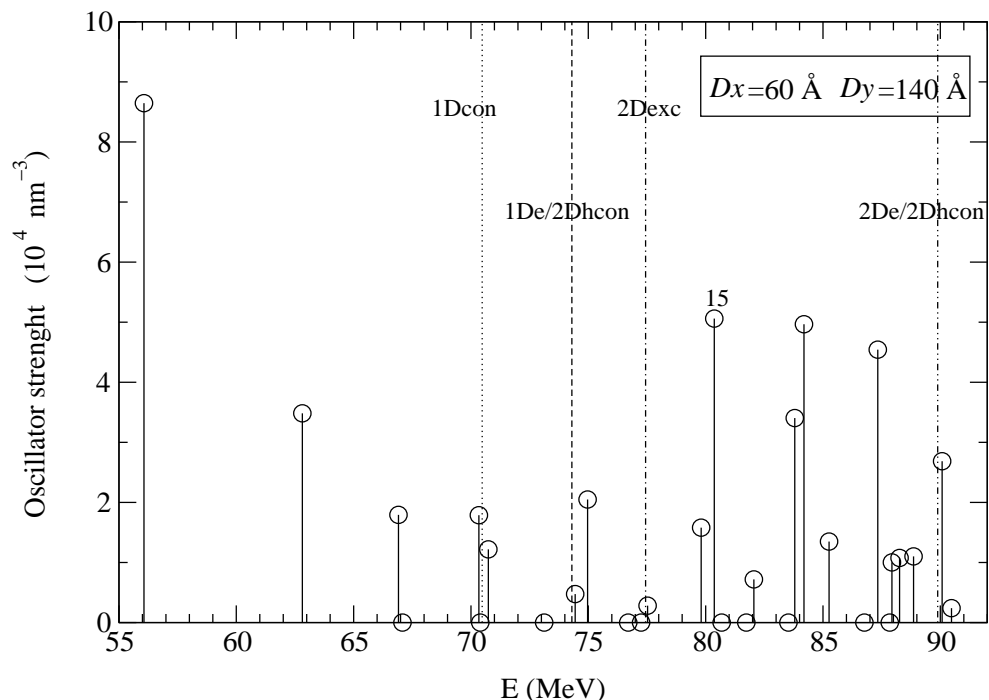


Figure 2.5: Oscillator strength versus energy for the lowest 30 states in an asymmetric T-shaped structure with $Dx = 60 \text{ \AA}$, $Dy = 140 \text{ \AA}$.

similar to the case of the symmetric wire. The first two excited states are exciton-like and have an electron confined in the wire while the hole spreads into the well. All excited states up to the 20th have the electron confined in the wire. The hole spreads to one or both quantum wells taking up more energetic states in the well. The relative coordinates show either an exciton-like wave function (states with nonzero oscillator strength in the spectra

of Figure 2.5) or the case where a hole is confined in the wire but is not bound to the electron (states with zero oscillator strength in the spectra). Both groups were discussed and shown for the symmetric wire.

The 21st and the 24th states (large oscillator strengths in the Figure 2.5) have an electron expanding into the Arm well. The electron wave function has a node in the wire region. The hole wave function spreads into the Arm well and has no node for the 21st state and one node in the wire region for the 24th state. The relative coordinates show the excitonic nature of these states. Thus these states correspond to those 2D excitonic states scattered on the wire.

For the asymmetric structure we observe one state (the 15th, see Figure 2.6) which does not correspond to any state in the symmetric case. The state is clearly excitonic-like with a large oscillator strength and the relative coordinate plots show a very well bound exciton. The electron is confined in the wire in the same way as the ground state while the hole is clearly 1D-like, strongly confined in the wire but in a different way. It has a node in the wire region.

2.2.2 Trends in Confinement and Binding Energies

Symmetric Wires

We calculate the exciton binding energy, $E_b = E_e + E_h - E_{1Dexc}$, where E_e and E_h are the one-particle energies of an electron and a hole, respectively, in the wire. We also calculate, using the same method, the exciton energy in the quantum well, E_{2Dexc} , to obtain the confinement energy of the 1D exciton, $E_{con} = E_{2Dexc} - E_{1Dexc}$, in the wire. We perform calculations for a wide range of structural parameters. For the GaAs/Al_xGa_{1-x}As quantum wire we change the well width from 10 Å to 80 Å for three different values of the Al content x . The results are shown in Figure 2.7. It can be noticed that for a well width bigger than 50 Å, changing the Al content has very little effect on the confinement and binding energies. The difference in binding energy between the 60 Å GaAs/Al_{0.35}Ga_{0.65}As and the pure AlAs is only 1.5 meV. Thus it seems more promising to change the well width rather than the Al content for relatively wide wires. However, for thinner wires in the range of 10-50 Å, changing the Al content is much more profitable than changing the well width. The difference in binding energies for 20 Å wires with Al molar fractions of $x=0.3$ and $x=1.0$ is 6.4 meV. This increases to 10.6 meV when the width is reduced to 10 Å.

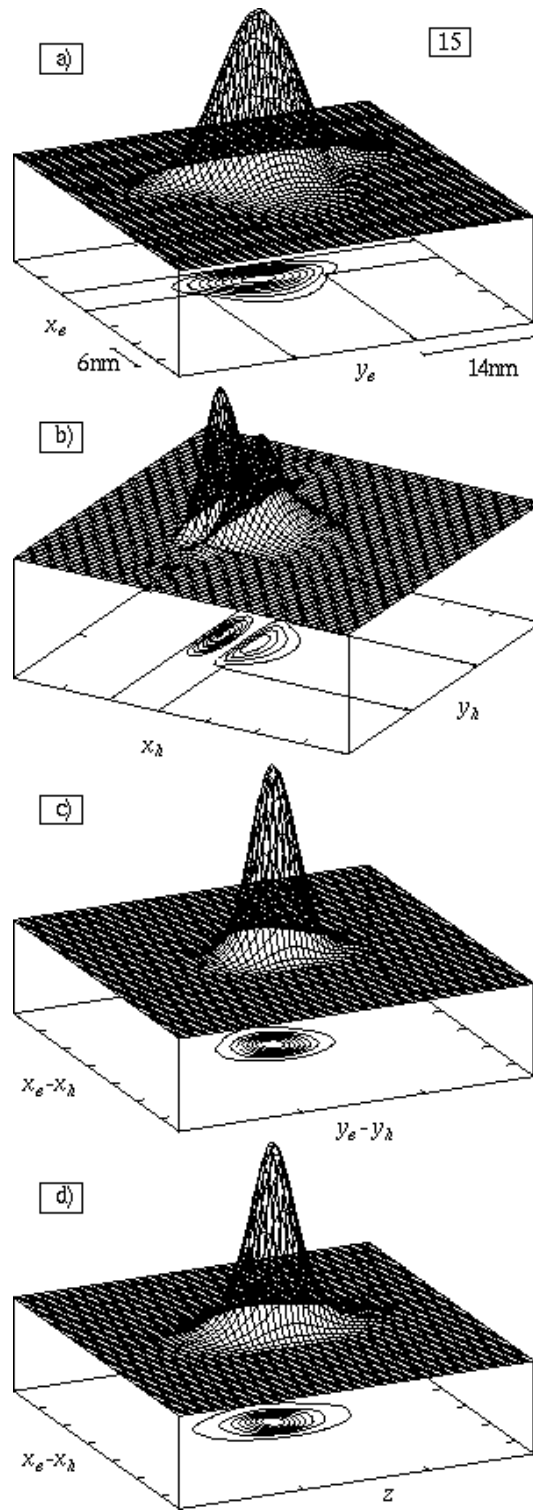


Figure 2.6: Electron (a), hole (b), and the relative coordinates $x_e - x_h$, $y_e - y_h$ (c), $x_e - x_h$, z (d) probability densities for the 15th state in an asymmetric T-shaped structure with $Dx = 60 \text{ \AA}$, $Dy = 140 \text{ \AA}$.

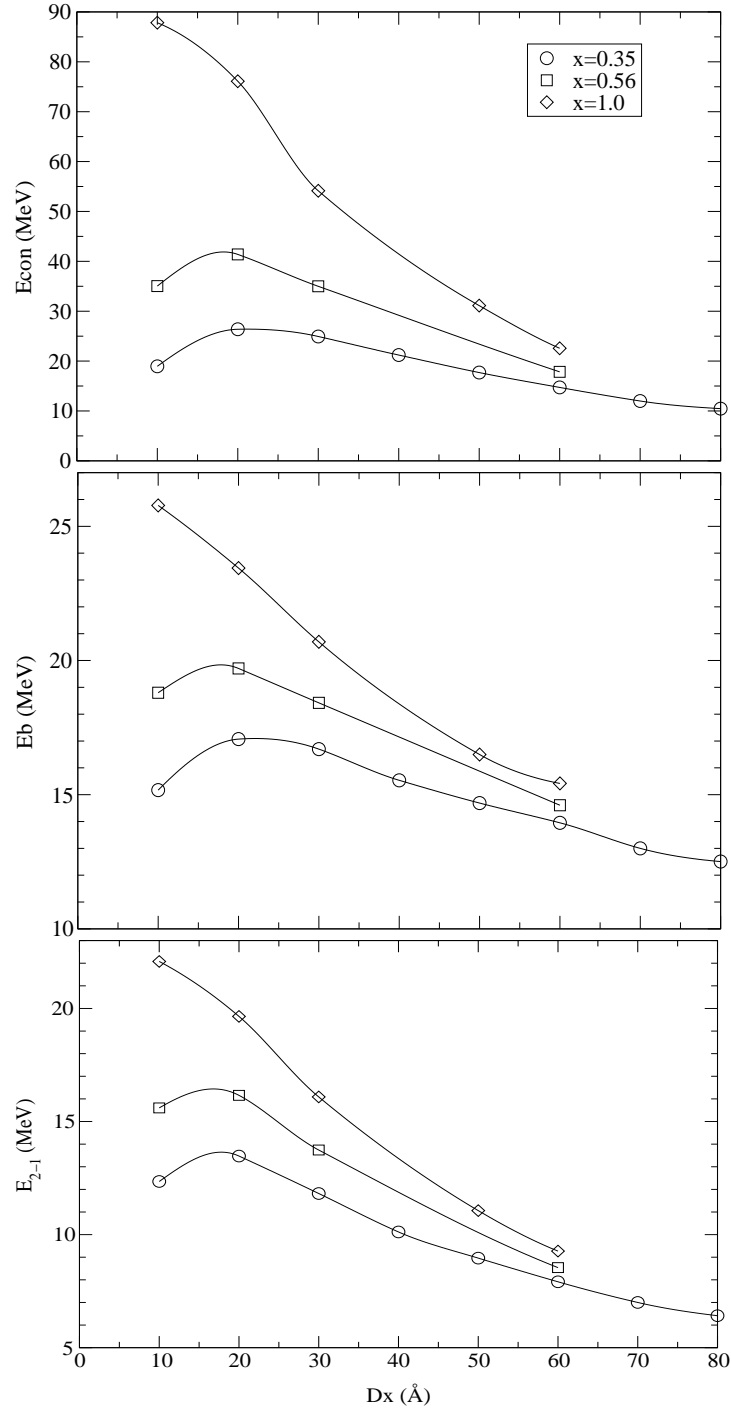


Figure 2.7: Confinement energy $E_{con} = E_{2Dexc} - E_{1Dexc}$, binding energy of the ground-state exciton E_b , and the energy difference between the ground state and the first excited state E_{2-1} as a function of the well width Dx in a symmetric T-structure for three different aluminium molar fractions x .

E_b and E_{con} for Al contents of $x=0.35$ and $x=0.56$ both approach a maximum for a well width between 10 \AA and 20 \AA . The maximum values for $x=0.35$ are $E_{bmax} = 17.1 \text{ meV}$, $E_{conmax} = 26.4 \text{ meV}$ and for $x=0.56$ they are $E_{bmax} = 19.7 \text{ meV}$, $E_{conmax} = 41.4 \text{ meV}$. For the $x=1.0$ case, the curve does not have a maximum in the region for which calculations has been performed but we consider going to wells thinner than 10 \AA as practically uninteresting. Thus the maximum energies are for $Dx=10 \text{ \AA}$ and they are $E_{bmax} = 25.8 \text{ meV}$ and $E_{conmax} = 87.8 \text{ meV}$.

E_{con} increases much more rapidly than E_b when the well width is progressively reduced. The curves cross for a well width between 60 \AA and 70 \AA , i.e. for widths of 60 \AA or smaller, E_{con} is greater than E_b which means that the 1D continuum is lower in energy than the 2D exciton (as we discussed in section 2.2.1) with the difference having a maximum at around 20 \AA . For widths of 70 \AA or bigger, E_b is greater than E_{con} with the difference growing for increasing well width. We also consider the difference in energy between the ground state exciton in the wire and the first excited state as a function of the well widths. For the experimentally realised $Dx = 70 \text{ \AA}$ case, this difference is $E_{2-1} = 7.0 \text{ meV}$ and the maximum value for $Dx = 10 \text{ \AA}$ is $E_{2-1max} = 13.5 \text{ meV}$. The maximum value for the GaAs/AIAs at $Dx = 20 \text{ \AA}$ is 22 meV .

Although pure AIAs gives the biggest potential offsets and thus the biggest binding and confinement energies, the GaAs/AIAs interfaces are not very smooth, which influences the transport properties. Thus new materials have to be proposed. Two structures based on InGaAs have been manufactured and measured [2]: 35 \AA -scale $\text{In}_{0.17}\text{Ga}_{0.83}\text{As}/\text{Al}_{0.3}\text{Ga}_{0.7}\text{As}$ (N4) and 40 \AA -scale $\text{In}_{0.09}\text{Ga}_{0.91}\text{As}/\text{Al}_{0.3}\text{Ga}_{0.7}\text{As}$ (N2). The results of calculations for these structures are presented in Table 2.1. It can be seen that energies for the sample N4 are almost exactly the same as for the GaAs/AIAs sample S2 suggesting that these materials might be very good candidates for structures with large exciton confinement and binding energies.

Asymmetric Wires

In order to increase binding and confinement energies, the asymmetric T-shaped structure was proposed and realised by two groups [4, 5, 8].

We calculate E_b and E_{con} for the $60 \text{ \AA}/140 \text{ \AA}$ structure with the Stem quantum well filled with 7% Al in order to compare with experiment [8] and then we vary the width of the Arm well from 50 to 100 \AA . One can see from Figure 2.8 that the binding energy is almost independent of the Arm well width in this region, changing only from the maximum value

of 13.5 meV for $Dx = 60 \text{ \AA}$ to 11.5 meV for $Dx = 100 \text{ \AA}$. The binding energy for the 60 \AA

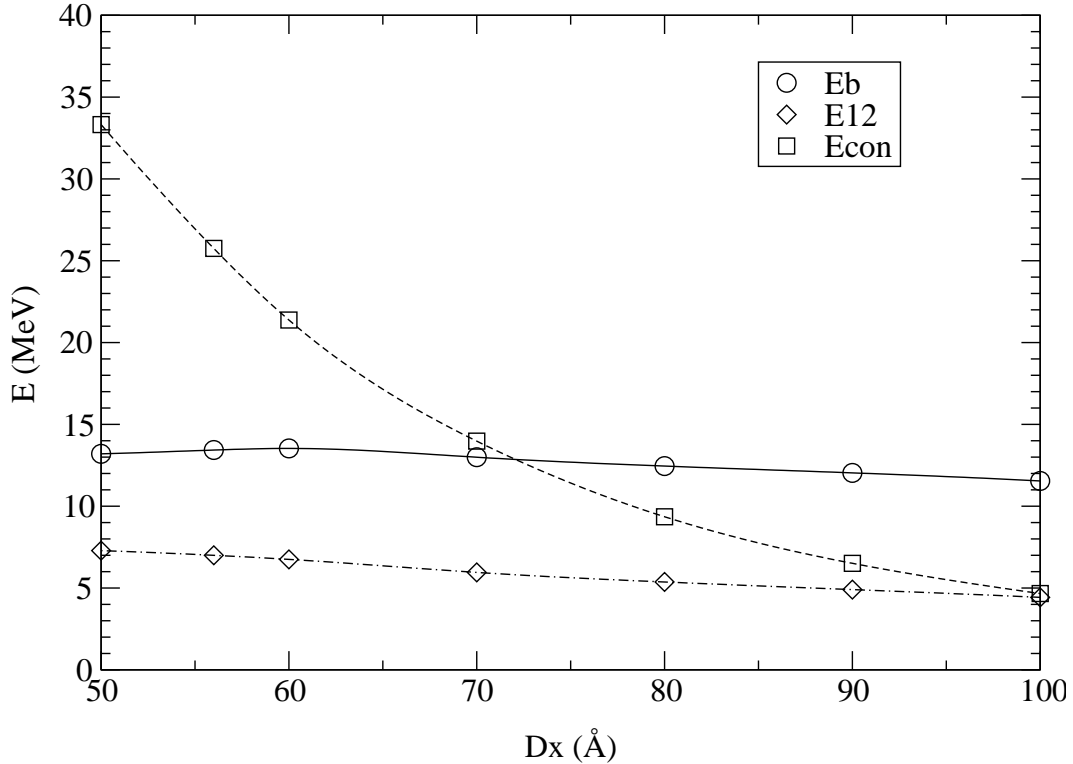


Figure 2.8: Confinement energy $E_{con} = E_{2Dexc} - E_{1Dexc}$, binding energy of the ground state exciton E_b , and the difference between the ground and the first excited state E_{2-1} for an asymmetric wire as a function of the well width Dx , where $Dy = 140 \text{ \AA}$.

symmetric wire with the same $x=0.35$ Al mole fraction is 13.9 meV - a bit bigger than for the asymmetric structure. In contrast, the confinement energy, E_{con} , changes rapidly with the width of the Arm well from 4.7 meV for $Dx = 100 \text{ \AA}$ up to 33.3 meV for $Dx = 50 \text{ \AA}$. For Arm-well widths of 60 \AA or bigger, the 2D quantum-well exciton in the Arm well has a lower energy than that for the Stem well, thus the confinement energy is calculated with respect to the Arm well exciton. For the 50 \AA -wide Arm well, the 2D exciton has higher energy than for the Stem quantum well and thus the confinement energy is calculated with respect to the Stem quantum well. Therefore 33.3 meV is the highest confinement energy for this Stem well and changing the Arm well would have no effect. Thus the $60 \text{ \AA}/140 \text{ \AA}$ structure is well optimised and its confinement energy, E_{con} , is 21.4 meV which is much bigger than that of 14.7 meV for the 60 \AA symmetric wire.

The highest confinement energy so far reported is for an asymmetric GaAs/Al_{0.35}Ga_{0.65}As wire with a 25 \AA Arm quantum well and a 120 \AA Stem quantum well filled with 14% Al [4,5].

The experimentally obtained E_{con} for this structure is 54 meV. Our calculations however give only 36.4 meV which is still the highest among experimentally obtained structures but much lower than reported by the authors. Our calculation of E_{con} for five different experimentally realised structures agree very well with the experimental values and thus it is very probable that the value of 54 meV is overestimated. The binding energy from our calculations is only 14.6 meV for this structure.

We can conclude from our results that the optimised asymmetric structure does not lead to a bigger exciton binding energy than the symmetric ones with the same parameters. The confinement energy is considerably enhanced and this effect, which can be measured directly, has often been used to infer that the binding energy is increased. However, our results show that no such relationship holds between the confinement and binding energies. Thus the biggest confinement energy of any structure constructed so far of 36.4 meV does not lead to the biggest binding energy. Indeed, the binding energy of 14.6 meV is smaller than the 16.5 meV reported for the GaAs/AlAs 50 Å-scale symmetric structure [3] where the confinement energy should be only 31.1 meV. It is also smaller than expected for a symmetric 25 Å-scale structure with the same parameters (16.0-16.5 meV). Thus asymmetric structures could be useful for applications where a large confinement energy is required but appear to be less suitable than symmetric wires for applications where large binding energies are of interest.

Comparison with Experiment and Other Calculations.

The comparison between experiment and other published calculations is presented in Table 2.1. The confinement energy of the exciton can be directly measured experimentally. Although, due to the strong inhomogeneous broadening of the photoluminescence peaks, the accuracy of this number is not very high, it is the only experimentally proven quantity we can refer to. The experimental binding energy needs to be calculated using both experimental data and one-particle calculations and thus errors might accumulate. Other theoretical methods which we refer to obtain the ground state exciton energy using variational techniques [12]- [14] (they differ in the form used for the variational wave functions). There are also two non-variational calculations for the ground state exciton [10, 11].

Table 2.1: Binding energy, E_b and the confinement energy $E_{con} = E_{1Dexc} - E_{2Dexc}$ in meV of the QWR exciton for seven different samples W, S_1, S_2, N_2, N_4, R and G obtained from different methods.

Method	W^a		S_1^b		S_2^b		N_2^c		N_4^c		R^d		G^e	
	E_b	E_{con}	E_b	E_{con}	E_b	E_{con}	E_b	E_{con}	E_b	E_{con}	E_b	E_{con}	E_b	E_{con}
Exp ^f	17	17	17	18	27	38		28		34	13.8	23		54
This work	13	12	14.3	17.8	16.5	31.1	12.1	26.3	16.5	31.2	13.5	21.4	14.6	36.4
Nonvar1 ^g	13.2		14.3		16.4									
Nonvar2 ^h			11.63		13.9									
Var1 ⁱ			15		18									
Var2 ^j	9.6	11.9												
Var3 ^k	12	14												

^a Sample and experimental values from Ref. [6].

^b Sample and experimental values from Ref. [3].

^c Sample and experimental values from Ref. [2].

^d Sample and experimental values from Ref. [8].

^e Sample and experimental values from Ref. [4, 5].

^f E_{con} is obtained experimentally from the shift between QW and QWR exciton lines.

The E_b is obtained indirectly from experimental measurement of the QWR exciton line and one-particle calculations.

^g Results of calculations from Ref. [10].

^h Results of calculations from Ref. [11].

ⁱ Results of variational calculations from Ref. [12].

^j Results of variational calculations from Ref. [13].

^k Results of variational calculations from Ref. [14].

Our results for the confinement energy of the ground state exciton E_{con} agree very well with experimental values for samples S1, N2 and N4 to an accuracy of 1%, 6% and 8% respectively. This is indeed very good agreement taking into account the strong inhomogeneous broadening of the peaks they present. The spectral linewidth of the photoluminescence peaks according to the authors is around 15 meV which corresponds to a thickness fluctuation of about 3 Å for N2 and N4 [2]. For the S1 and S2 samples the authors estimate the experimental error due to the inhomogeneous broadening as 2 meV. Agreement between our calculations and experiment is not as good for the S2 sample but for this case additional effects are present. For example, AlAs barriers give much less smooth interfaces than the lower Al fraction samples and this is not taken into account in our model. There is also very good agreement (better than 7%) between our results and the experimental measurement [8] for asymmetric wire R. The earlier E_{con} published by this group for the symmetric structure W is probably slightly overestimated.

All calculations published to date use the effective mass approximation model for the heavy-hole exciton. Values of potential barriers used in the calculations vary depending on the publication. We have examined the influence of these differences on the final results (see Section 2.2.4). Both binding and confinement energies can differ by approximately 0.5 meV

There are only two calculations published for the confinement energy. They are based on variational methods and were performed only for sample W. Variational method 2 [13] uses a wave function which takes into account correlation in all spatial direction and the agreement with our results is very good for the confinement energy but not so good for the binding energy.

The variational method proposed by Kiselev et al. [14] and denoted here by “3” has a trial wave function which has only z dependence in the correlation factor. Their binding energy for the sample W differs by only 1 meV from our result but their value for the confinement energy differs from ours. They perform calculations of the binding energy for the whole range of well widths, Dx , from 10-70 Å. This can be compared with our results in Figure 2.7. Their calculations, like ours, give the maximum for E_b and E_{con} for a well width of around 20 Å. Their binding energy is a bit bigger than the one from our calculations. They obtained a maximum of $E_b = 18.6$ meV which is 1.5 meV higher than our result. However, their confinement energy $E_{con_{max}} = 33.0$ meV differs by 7 meV from our result. Their values of E_{con} are probably overestimated. They use the variational technique to calculate the quantum wire exciton energy but the quantum well exciton

energy is taken from some other calculations of excitons in quantum wells performed using a different method and with different parameters, thus errors may accumulate.

The variational method 1 [12], which uses yet another form of trial wave function, has been applied to samples S1 and S2 to calculate the binding energy E_b . It agrees quite well with our and other accurate methods.

The binding energy we obtain shows excellent agreement with another non-variational calculation by Glutsch et al. [10] (see Table 2.1). They calculated the binding energy only for samples W, S1 and S2 and thus unfortunately the confinement energy cannot be compared. The method presented in reference [11] gives much lower values for the binding energy than all other methods.

Despite some small differences, all of the theoretical methods give much smaller values for E_b than the experimental estimates. One has to bear in mind, however, that the “experimental” values for E_b (quoted in the Table 2.1) are in fact derived from a combination of experimental data and associated theoretical modelling, with inherent uncertainties. Our results come from direct diagonalisation and are very well converged. Therefore we believe that the experimental binding energies are, in some cases, considerably overestimated. The real binding energy is thus smaller than has been claimed and the biggest value for any of the structures manufactured so far is 16.5 meV for samples S2 and N4.

2.2.3 Optimisation of Confinement Energy for Experimental Realisation

In Section 2.2.2 we have shown that for symmetric GaAs/Al_xGa_{1-x}As wires the upper limit for the binding energy is around 25 meV. We have also shown that in asymmetric structures, the confinement energy is enhanced with respect to the symmetric forms with comparable parameters but the binding energy of the exciton is then lower than in the symmetric structures. The upper bound of 25 meV is too low for the room temperature applications. There are some indications (Section 2.2.2) that In_yGa_{1-y}As/Al_xGa_{1-x}As might be a good candidate.

Good quality GaAs/Al_xGa_{1-x}As wires are, however, much easier to manufacture than the In_yGa_{1-y}As/Al_xGa_{1-x}As ones, which brings a considerable interest in optimising the confinement energy for the GaAs/Al_xGa_{1-x}As wires. The form of the density of states for electrons and holes in 1D (see Chapter 1) is very useful for low-threshold laser applications. Therefore structures in which excitons dissociate at room temperature but remain in the wire would also be relevant for practical applications.

We collaborate with experimentalists from Bell-Laboratories to design such lasers. The optimisation of the confinement energy of excitons is a crucial issue in this design. We have shown in Section 2.2.2 that in the asymmetric T-shaped wires, the confinement energy is enhanced with respect to the symmetric forms, with comparable parameters. We will try now to optimise the GaAs/Al_xGa_{1-x}As asymmetric wires within the well thickness and Al concentration range accessible by experiment.

We perform calculations for structures shown in Figure 1.2 with a 140 Å, 120 Å and 100 Å Stem well filled with 7 %, 10 % and 13 % Al respectively. For all four different Stem wells we vary the width of the Arm well for four different potential barriers corresponding to 100 %, 70 %, 50 % and 35 % of Al content. The Arm well width is varied from 90 Å to around the value for which E_{con} has a maximum. For each structure this maximum corresponds to the case in which exciton energies in the Arm and Stem quantum wells are equal. When the width of the Arm well is decreased further the Arm well exciton energy increases, causing the exciton to spread more into the Stem well and reducing the quantum confinement.

The binding energy of excitons does not vary much within the studied range and it changes from 17 meV for a wire which consists of a 100 Å/ 13 % Stem well, 40 Å Arm well and 100 % Al barriers to 12 meV for a wire with a 140Å/ 7 % Stem well, 90 Å Arm well and 35 % Al barriers. The values of E_b for these wires are also slightly smaller than for the corresponding symmetric structures (see Figure 2.8 - upper panel). The confinement energy, however, is much enhanced with respect to the symmetric forms (see Figure 2.8 - middle panel) and strongly depends on its parameters. The results of our calculations for E_{con} are shown in Figure 2.9. We now discuss the general trends for the confinement energy.

The highest confinement energies can be achieved for the 100 Å/ 13 % Stem well (black curves in Figure 2.9), then for the 120 Å/ 10 % (red curves) and finally for the 140Å/ 7 % Stem wells (blue curves). However the maximum value of E_{con} corresponds to a different Arm well width for each different Stem well. Notice that this maximum corresponds to a 30-40, 40-50, 50-60 Å Arm well width for the 100 Å/13 %, 120 Å/ 10 %, and 140Å/ 7 % Stem well respectively. Thus although with a 100 Å/13 % Stem well we can achieve the highest confinement energies we need to manufacture the thinnest Arm wells to achieve this. On the contrary for wider Arm well the highest E_{con} can be achieved with the 140Å/ 7 % Stem wells.

It could be possible to introduce yet different types of Stem well to increase E_{con} even

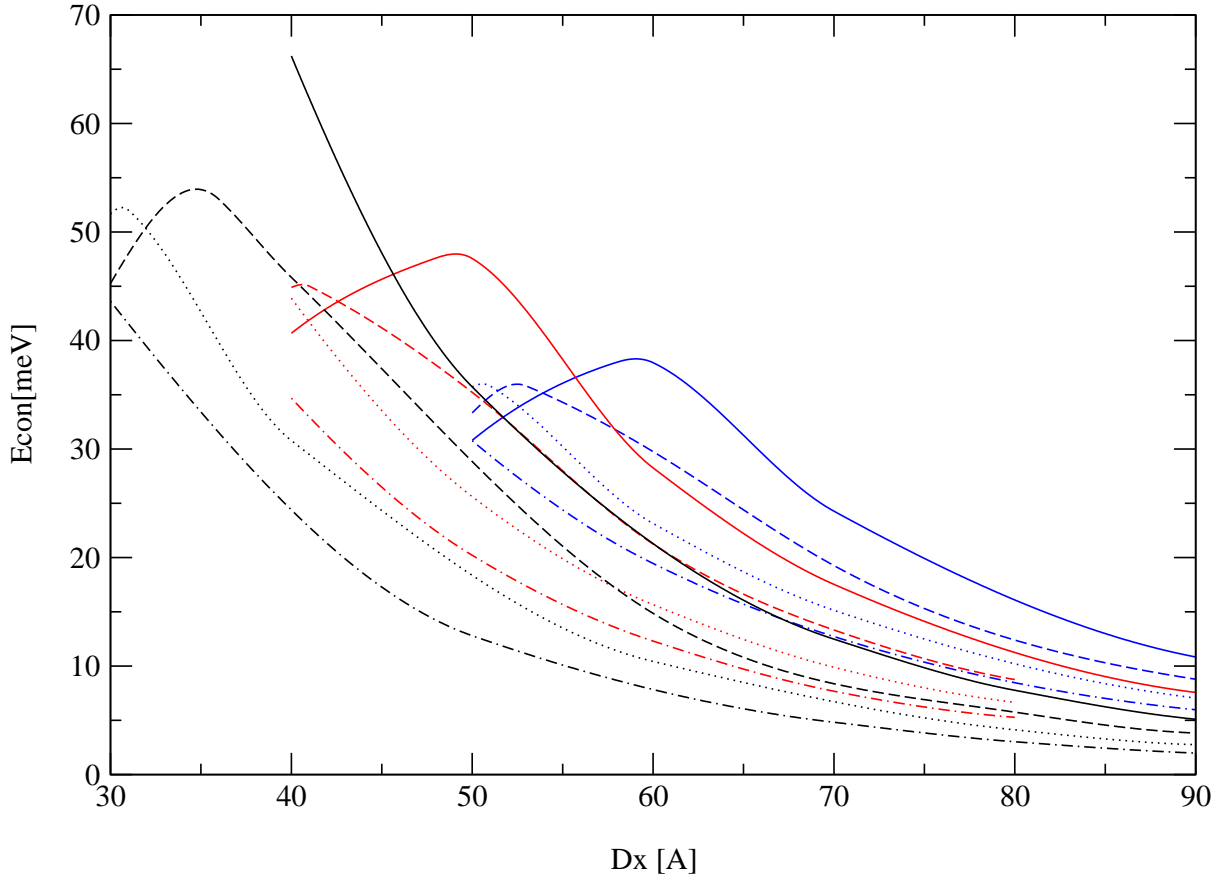


Figure 2.9: Confinement energy $E_{con} = E_{2Dexc} - E_{1Dexc}$ for asymmetric wires as a function of the Arm well width Dx , for different Stem wells and potential barriers. Blue curves correspond to the 140Å/ 7 % Stem well, red curves to the 120 Å/ 10 % and black curves to the 100 Å/ 13 % Stem well. Solid lines are for 100 % Al barriers, dashed lines for 70 % Al, dotted lines for 50 % Al and dashed-dotted lines are for 35 % Al barriers.

further. Unfortunately, the higher E_{con} could only be achieved by using Arm wells thinner than 30 Å which would not be practical. The dependence of E_{con} on the Al content in potential barriers is the simplest one. E_{con} always increases with an increase of Al content.

Although generally the value of the confinement energy is highest for high Al contents and thin Arm wells both these features bring additional experimental difficulties [18]:

- For higher Al concentration, yields of cleavage in CEO become worse and interfaces get rougher which degrades the transport properties.
- Above 50% AlGaAs becomes an indirect-gap semiconductor.

- It becomes harder to make an optical wave guide for a laser structure with higher Al concentration.
- Thinner Arm-QWs cause higher thresholds in lasing.
- In thinner QWs the wavefunctions tends to penetrate deeply into AlGaAs, which may reduce the photoluminescence.

In optimising wires for practical applications one needs to take into account both the above mentioned difficulties and the gain in the confinement energy. The detailed calculations of E_{con} for a wide range of structures are therefore very important. Our calculations are being used to design quantum wire lasers which would operate at room temperature. This work, in collaboration with Bell-Laboratories, is still in progress.

2.2.4 Accuracy of the Results

In our method the one-particle energies and wave functions are calculated first. The one-particle energies are very well converged with respect to all the variables such as unit cell size, number of points on the grid and the number of plane waves to an accuracy of 0.1 meV. We use on average as many as 160 000 plane waves which corresponds to 400×400 points on the grid (200×200 in the small unit cell). We obtain excellent agreement between our energies for the single electron and hole and those obtained by Glutsch et al. [10]. For the 70 Å, $x=0.35$ symmetric quantum wire we obtain $E_e = 47.09$ meV and $E_h = 7.47$ meV while their results are $E_e = 47.2$ meV and $E_h = 7.5$ meV. According to our calculations there is only one electron state confined in the wire and its confinement energy E_{2D-1D} (i.e., the difference between well-like and wire-like electron states) is 9 meV. This is in very good agreement with other methods. L. Pfeiffer et al. [15] using eight band $\vec{k} \cdot \vec{p}$ calculations obtained a confinement energy of 8.5 meV for the same structure. Kiselev et al. [14] using the so-called free-relaxation method obtained approximately the same value of 9 meV.

These one-particle wave functions are then used as a basis set for the two-particle calculations. The E_{1Dexc} is very well converged with respect to the number of points on the grid (as for the one-particle calculations), and with the size of the basis set (see Appendix A, Tables A.1 and A.2). Convergence is usually achieved with about $20 \times 20 \times 20$ (8000) basis functions. In order to minimise finite size effects we use quite big unit cells (from 43 times the well width, Dx for very thin wires (10 Å) to 7 times Dx for the 80 Å wire). The exciton energy E_{1Dexc} is converged to within about 0.2 meV and E_{2Dexc} to

within 0.3 meV which gives an accuracy for E_b of about 0.3 meV and for E_{con} of about 0.5 meV.

The other problem which can influence the accuracy of the results is the uncertainty associated with the input parameters. The electron and hole masses as well as the dielectric constant are standard but the potential barriers vary a lot depending on the publication. We have found quite different values of the potential offsets for the same material interfaces in the literature. We have examined the influence of this uncertainty on the final results by performing calculations for the extrema of the sets of parameters found. Both binding and confinement energies can differ by approximately 0.5 meV.

For the parameters that we are using, the results are converged to within 0.3 meV for the binding and 0.5 meV for the confinement energies. However, one needs to remember that these parameters are not well calibrated and this could lead to an additional error in both energies of about 0.5 meV.

The first few (4 in the case of Fig 2.5) excited states of the wire which are below the 1Dcon and the 2Dexc are discrete, quasi-1D excitonic states and are converged to within 1 meV. Convergence of the higher states in the continuum is more complicated. Because our system is finite we obtain only a sampling of the continuum states. When we increase the unit cell size we automatically calculate more states within the same energy region and they do not have a one to one correspondence with the states calculated using a smaller unit cell. The new states appear in between the old ones, with smaller oscillator strengths so that the total oscillator strength is conserved. When the Gaussian broadening of a 4 meV (FWHM) is added to the spectra then for a sufficiently big unit cell the broadened spectrum is independent of the unit cell, thus convergence is reached (see Appendix A, Figures A.1 and A.2). The spectra shown in Figs 2.2 and 2.5 are converged in the sense that the continuum is accurately sampled on the scale of 4meV.

2.3 Conclusions

We have performed an exact diagonalisation within a finite basis set of the Hamiltonian which describes an interacting electron-hole pair in a T-shaped quantum wire. We have obtained the ground and excited state energies and wave functions for this system. The first group of excited states shows an *s*-like excitonic character where the electron is localised in the wire but is bound to the hole which spreads into one of the wells. Due to the fact that the electron and hole are not localised in the same region, we have a group of low

oscillator-strength states just above the ground state. This group is followed by a number of states with large oscillator strength which are 2D excitonic states scattered on the T-shaped intersection. The excitonic lasing from one of those states has been experimentally observed [8]. We have also performed a detailed study of the exciton binding and confinement energies as a function of the well width and Al molar fraction for symmetric and asymmetric wires. The highest binding energy in any structure so far constructed is calculated to be 16.5 meV which is much smaller than previously thought. Our results have shown that for optimised asymmetric wires, the confinement energy is enhanced but the binding energy is slightly lower with respect to those in symmetric wires. For GaAs/Al_xGa_{1-x}As wires we have obtained an upper limit for the binding energy of around 25 meV in a 10 Å wide GaAs/AlAs structure which suggests that other materials need to be explored in order to achieve room temperature applications. In_yGa_{1-y}As/Al_xGa_{1-x}As might be a good candidate.

Chapter 3

Two-mode Excitonic Lasing in T-shaped Quantum Wires

In this Chapter we present the experimental observation of two-mode lasing in asymmetric, T-shaped quantum wires [8]. Under strong excitation the simultaneous lasing from two levels in the structure is achieved. We then apply the numerical calculations described in Chapter 2 for structures used in this experiment and identify the origin of the two laser modes.

3.1 Experimental Set-up

The laser structure studied experimentally consists of two intersecting quantum wells fabricated by cleaved edge overgrowth molecular beam epitaxy (MBE). One set of quantum wells called Stem wells are grown on a (001) GaAs substrate, and then in a second MBE growth an intersecting Arm quantum well is grown on the (110) crystal face exposed after an in situ cleave of the GaAs wafer in the growth chamber (see Fig. 1.2). Previously reported work studied a symmetric configuration in which Arm and Stem quantum wells had the same width [6]. The work described here is in an asymmetric structure, where the Stem well is significantly wider but filled with low percentage AlGaAs to compensate for the reduction in confinement energy. The structure is composed of 20 Stem QWs, 140 Å wide with a 7 % Al content intersecting a single 56 Å or 60 Å GaAs Arm QW to form the T-QWRs. These 20-wire structures are embedded in a multilayer arrangement that forms an optical cavity whose fundamental mode concentrates the emitted light around the quantum wires. A detailed description of the optical cavity can be found [6]. Along

the wire axis, the 500 nm long laser cavity is limited by two additional (011) cleaved surfaces that are left uncoated. The carriers are resonantly excited by optically pumping the Stem quantum well adjacent to the wire intersection. These carriers populate the Stem wells and after phonon emission [19], they relax to wire states and eventually recombine. The enlarged absorption length associated with the wider stem wells in this sample results in much larger carrier generation than in previous T-wire laser devices. This manifests itself also in a x4 reduction of laser threshold power compared with symmetric structures. In what follows, the excitation power refers to that of the pump laser focused homogeneously over the whole optical wire cavity area, and a maximum pump power of 500 mW corresponds to a density of $\sim 2\text{kW}/\text{cm}^2$.

3.2 Experimental Data

The effect of changes in photoexcitation intensity on lasing and also on the spontaneous emission in these T-wire lasers is displayed in Fig. 3.1. Below threshold both the on- and off-axis spectra show the luminescence from the excitonic ground state of the wires at 1.570 eV. The luminescence from the Arm well appears as a weak shoulder in the off-axis emission but becomes more prominent as a second peak at 1.593 meV as the photoexcitation energy is raised. At 140 mW the sample is lasing in multimode with the gain centred at 1.567 meV (L1), an energy which is very close to the excitonic ground state of the wire. This photon energy is preserved for both kinds of emissions over the whole range of excitation powers. At pump powers above 300 mW a second lasing line (L2) appears and eventually dominates the laser emission. Simultaneous lasing at two lines in a single cavity implies a population inversion of more than one quantum state.

The positions of both laser lines remain largely constant, and L1 stays centred at an energy that is very close to that of the exciton at low excitation power. Given the accuracy in the measurement of the lasing line we can state that any shift is less than the spacing between adjacent cavity modes (0.3 meV). The observations seem to imply that laser gain displays excitonic behaviour even at the high excitation powers.

The switching between the L1 and L2 laser lines shown in Fig. 3.1 has the striking temperature dependence displayed in Fig. 3.2 [9]. At 40 K the sample is lasing in a well defined single mode at 1.57 eV. In the temperature range 50 - 60 K, when the pump power exceeds about 20 times threshold (see inset in Fig. 3.2), the drastic change in the laser emission occurs. The system becomes bistable with emergence of the second line (L2), blue

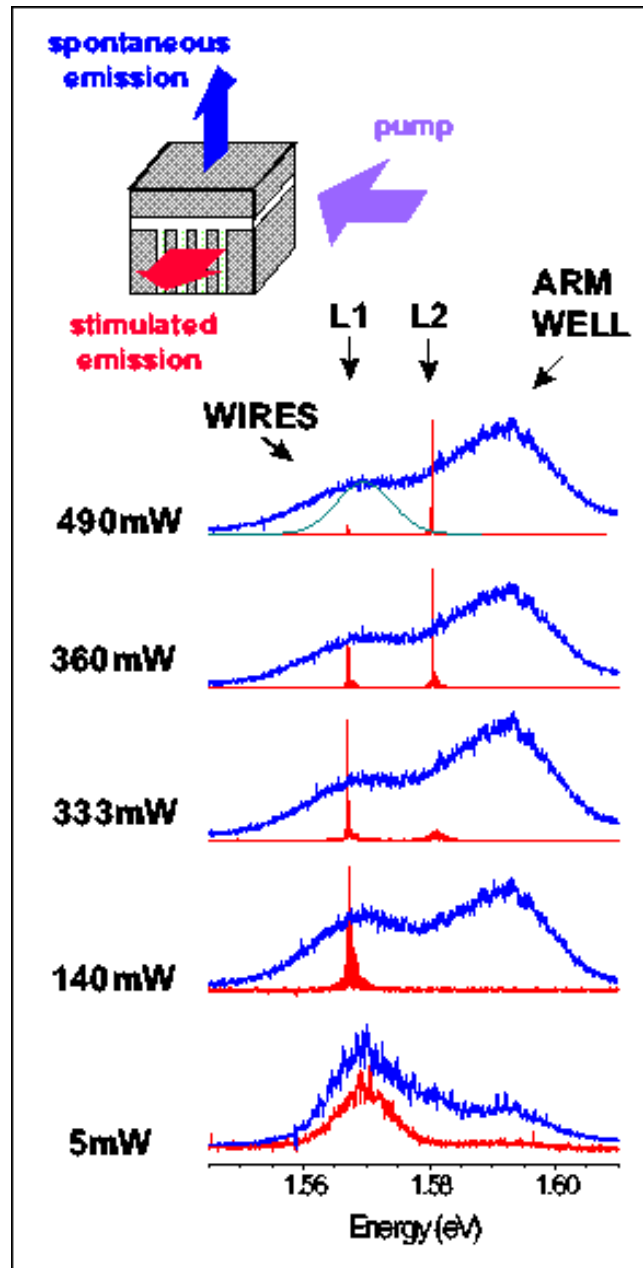


Figure 3.1: Spontaneous (blue) and stimulated (red) emission of the sample at $T = 65$ K for different excitation powers reflecting the influence of the pump power on the transition between L1 and L2 lasing lines. The spontaneous emission broadens to the high-energy side and develops a long low-energy tail with increasing power. To expose these effects a best fit of the QWR luminescence at the lowest power has been added to the spectra at 490 mW. The band at 1.593 eV is due to recombination associated with the 60 Å arm QW.

shifted 14 meV from the fundamental line (L1). Raising the temperature further causes the intensity of L1 to quickly diminish and the single mode lasing from the L2 lines is obtained. After the L2 line is established the threshold power begins to rapidly increase with temperature, causing the emission to decay into a multimode operation that persists to 80 K.

It has to be stressed that with increasing temperature the L1 line disappears, but with increasing pump power it saturates (when L2 turns on) and then slowly diminishes in absolute intensity.

Figure 3.3 presents the normalised difference of the two integrated intensities and shows that switching abruptly takes place within an interval $\Delta T \approx 5K$ around 55 K. At temperatures above 55 K the intensity of L2 increases monotonically with pump power, while L1 starts to diminish once both intensities become comparable. With the onset of L2 an increase up to 33 % in the slope can be measured as a kink in the response curve, in comparison with the gain saturation observed at lower temperatures where L2 is absent (see inset in Fig 3.3). These characteristics are suggestive of a phase transition, where carriers and photons are involved. A system of two lasing modes, represented by two coupled oscillators, has a rich phase diagram which will be expected to influence its photon statistics properties [20].

In the Figure 3.3 b the excitation spectra of both lasing modes are depicted for two temperatures. At temperatures below the transition (50 K), when only L1 is active, the excitation spectrum reproduces the expected absorption of the Stem well. But when both lasing lines are present, their intensities are strongly coupled as evidenced by the excitation spectrum at 57 K. Once L2 is activated, it competes with L1 to the point that the excitation spectrum of L1 develops a dip where L2 is maximum.

While the L1 line clearly corresponds to the excitonic ground state of the wires the origin of the L2 mode is not obvious. Since the binding energy of the exciton in this geometry is approximately 14 meV, one possibility might be exciton dissociation into itinerant quantum wire states. To distinguish possible scenarios another T-wire laser was studied with narrower Arm QW of 56 Å, which should have a nearly identical exciton binding energy, but a different energy level structure. In this sample a substantially higher L1 - L2 splitting of 17 meV was observed (see Fig. 3.4). The 20 % increased shift is not consistent with that exciton breakup hypothesis.

Since the L2 transition is only observed at high excitation levels the first suggestion was that L2 has entirely a many-body origin, connected with the presence of an electron-hole

plasma in the system. Such persistence of excitonic effects in 1D to high carrier density would be very remarkable.

Another possibility would be that the second lasing mode (L2) corresponds to a higher excitonic state in the structure.

Sorting out these possibilities represents a renewed challenge as there is no independent determination of the density. Both scenarios suggest that an upper limit for the density is approximately 1 per Bohr radius and thus is roughly of the order that one would expect for the transition from e-h plasma to bound excitons.

We have performed calculations which suggest that the L2 line corresponds to a higher excitonic state in the structure. We have first developed a rate equation model for the two-mode laser, presented in Chapter 4, assuming that the laser action takes place for two exciton-like states. This model can qualitatively reproduce the experimental data provided that the oscillator strength times the density of states for the upper excitonic state (L2 line) is higher than that for the ground state (L1 line). Motivated by this result we have performed detailed calculations for both structures studied in the experiment (56 Å and 60 Å Arm QWs) to identify the excitonic states which correspond to the two laser modes.

3.3 Calculations

We have performed numerical calculations of a single electron-hole pair in the T-shaped geometries of the two experiments to explore how the geometric changes might affect the spontaneous luminescence. To this end, we performed (see Chapter 2 and reference [21]) exact diagonalisations to determine not only the ground but also the excited states of the excitonic system, with results shown in Fig 3.5. The results for the two cases are similar: the ground state 1D exciton is bound 14 meV below the one-dimensional particle-hole continuum, and confined by 22 (26) meV in comparison to the 2D exciton in a 60 (56) Å arm well. There is an absolute shift of 3.5 meV in the 1D-exciton energy between the two structures, in agreement with experiment. We also find several excited states of the bound 1D exciton. States above the edge marking the free particle-hole excitation of the wire are of course in a continuum, and the discrete spectrum above 65 (69) meV is due to the finite box size of our calculations. We note that there is a broad peak of oscillator strength lying slightly above the 2D quantum well energy. Inspection of the wavefunctions of the large oscillator-strength states reveals that they are principally quasi-2D-exciton-like states strongly perturbed by the quantum wire potential, resonant with (and thus decaying

into) the continuum states of the wire. The oscillator strength of the 1D-continuum states themselves is weaker.

While these calculations are valid only for low density, the absence of substantial shifts in the luminescence spectrum with pumping suggests that the calculations can be used as a guide to the assignment of the transitions. L2 lies near but below the energy marking the onset of 2D excitons in the Arm well. Nevertheless, the shift of L2 from 14 to 17 meV between the 60 and 56 Å structures mirrors the calculated change of the exciton confinement energy in the wire from 22 to 26 meV, indicating that L2 may have well-like character.

Since the L2 transition is only observed at high excitation levels, it is possible that the 8-9 meV shift of the L2 line from the calculated 2D exciton edge may be a redshift induced by screening by the occupied 1D excitons.

Very recent experiments [22] give an additional support for the hypothesis that the L2 line is associated with the well excitons in the vicinity of the wires. With a reduction of a number of wires in the sample the threshold power for L1 lasing goes up while the threshold for L2 remains constant.

3.4 Conclusions

We have presented the experimental observation of two-mode lasing in asymmetric, T-shaped quantum wires [8]. Under strong excitation the simultaneous lasing from two levels in the structure was achieved. We have applied the numerical calculations described in Chapter 2 for both structures, with 60 Å and 56 Å Arm quantum well, used in this experiment to identify the origin of the two laser modes.

We have obtained an absolute shift of 3.5 meV in the 1D-exciton energy between the two structures, in agreement with experiment. We have also found several excited bound 1D exciton states but there is no evidence for emission from these states. Shift of L2 from 14 to 17 meV between the 60 and 56 Å structures mirrors the calculated change of the exciton confinement energy in the wire from 22 to 26 meV, suggesting that L2 has a well-like character, though the position of L2 is somewhat below the onset of 2D excitons in the arm well. Early suggestions that L2 is associated with emission from 1D e-h plasma are not substantiated.

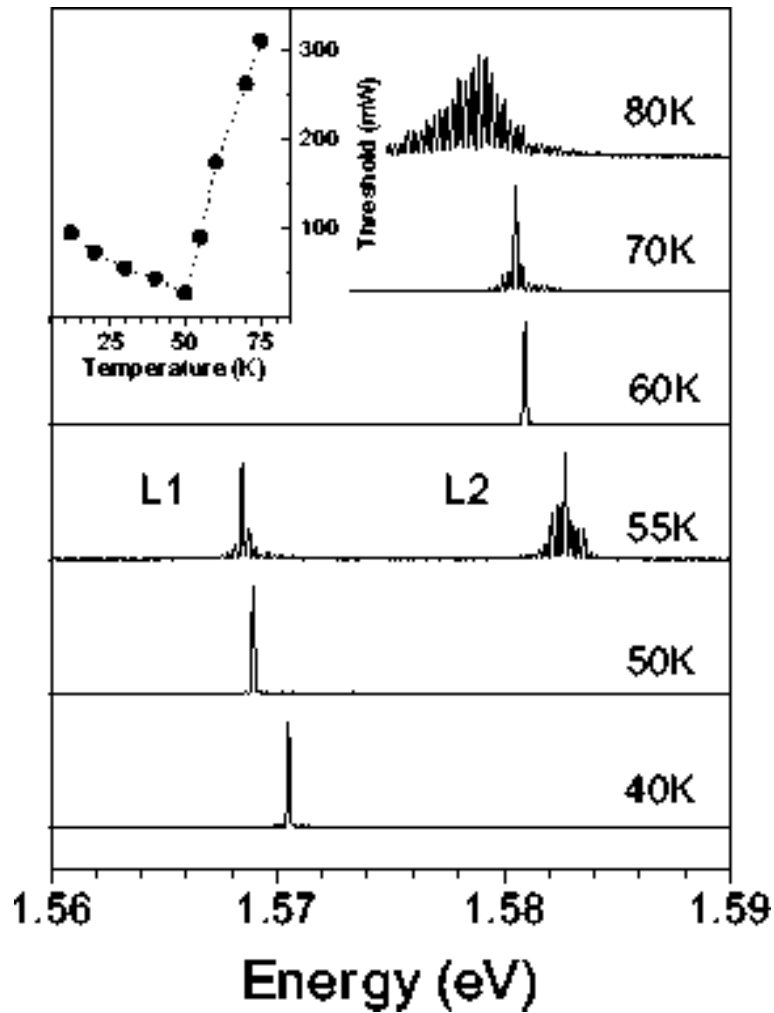


Figure 3.2: Stimulated emission from the multiple QWR laser structure with resonant optical excitation of 500 mW resonant with exciton peak of the Stem well absorption. The system becomes bistable at 55 K and switches to a new line displaced 14 meV in energy for higher temperatures. Inset: evolution of the threshold power with temperature.

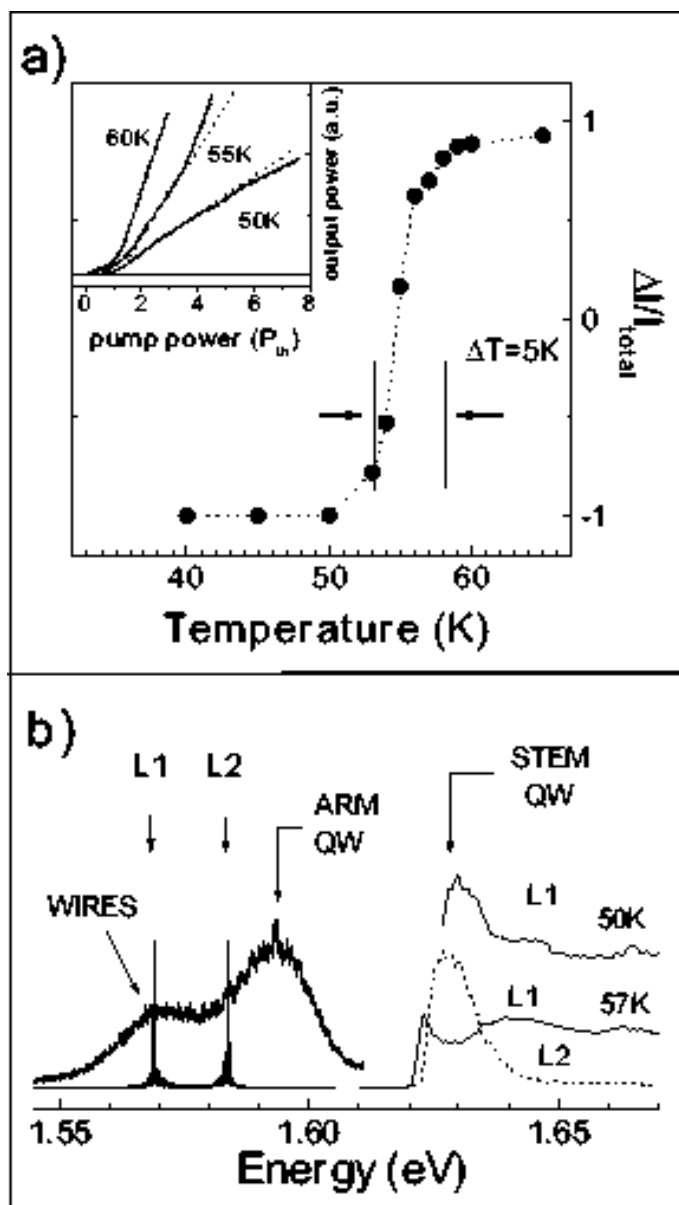


Figure 3.3: a) Normalised difference of integrated intensities $(I_{L2} - I_{L1})/I_{Total}$ as a function of temperature in the transition region. Inset: Laser intensity versus pump power for three temperatures near the transitions (the pump power is normalised to the threshold value at each temperature). The straight dotted lines are guides to the eye. b) Spontaneous and laser emission at 57 K and the separate excitation spectrum of the two laser lines for two different temperatures. The spectrum at 57 K reveals the strong coupling between the two optical transitions associated with L1 and L2.

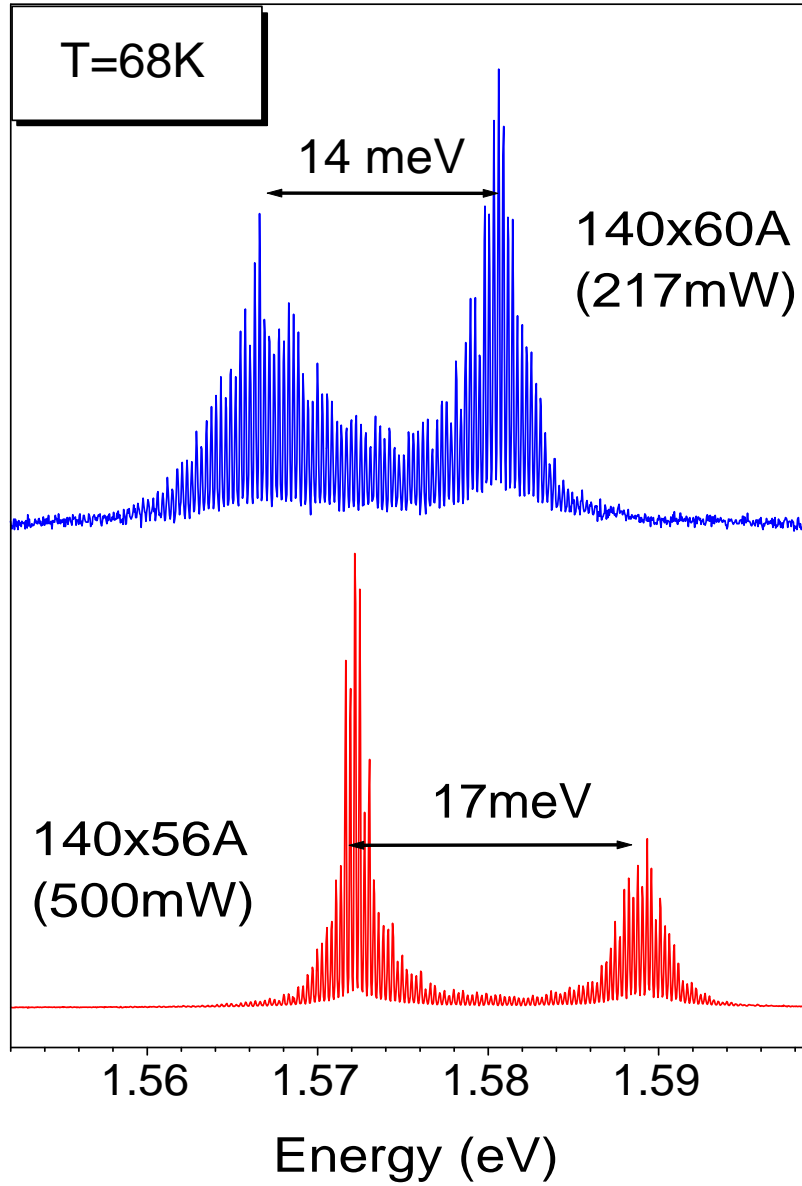


Figure 3.4: Stimulated emission from the multiple QWR laser structure with resonant optical excitation of 500 mW resonant with exciton peak of the stem well absorption, for two samples with arm well widths of 60 Å and 56 Å, otherwise identical. Both systems become bistable near 60 K and switch to a new line displaced 14 meV (17 meV) in energy for higher temperatures.

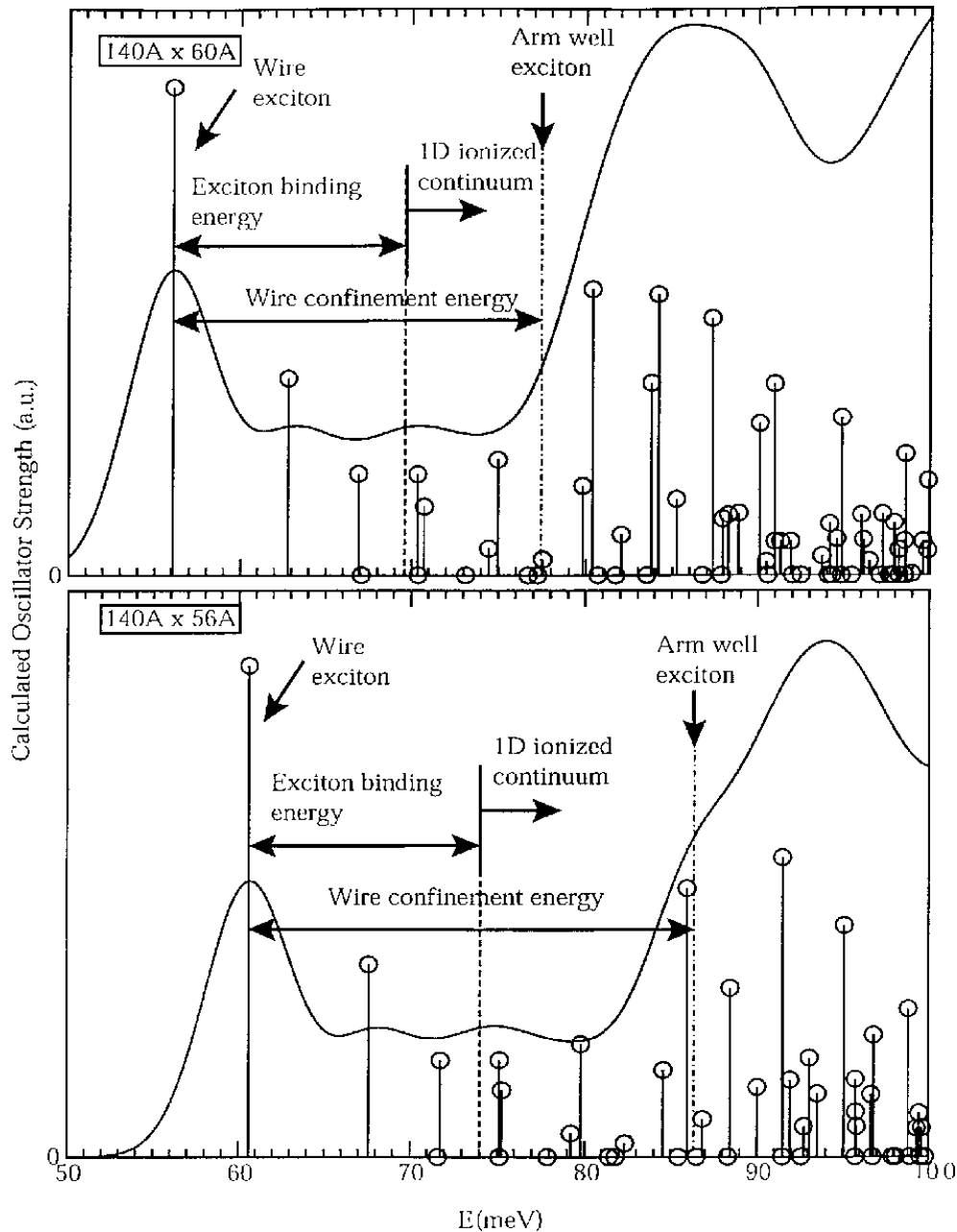


Figure 3.5: Calculations of the energies and oscillator strengths for ground and excited states of an electron-hole pair in the same two geometries as experiment. The onset of the 1D continuum of electron-hole plasma states, and the 2D exciton in the arm well are indicated. The solid line is produced by a Gaussian broadening with 3 meV HWHM, comparable to the inhomogeneous linewidth in the experimental system, and is meant as a guide to the eye. The peak in the oscillator strength above the 2D exciton edge arises because interactions with the wire perturb nonzero momentum excitons and make them optically active.

Chapter 4

Rate Equation Model for a Two-Mode Laser

In this Chapter we develop a rate equation model for a two-mode laser. Assuming that the laser action takes place for two different exciton-like states, we can reproduce the same qualitative behaviour of the laser, as observed in the experiment described in Chapter 3. The results of this Section support the hypothesis that the second lasing mode (L2) is associated with the higher excitonic state in the structure. The calculations of the spectra for experimentally studied wires (see Chapter 3) suggested that this higher excitonic state has a well-like character.

4.1 Experimental Motivations

In Chapter 3 we have described in detail the experimental observation of a two-mode lasing in asymmetric, T-shaped quantum wires. The first lasing mode comes from the ground state exciton while the nature of the second lasing line is not known. Determination of the origin of this line represents a renewed challenge as there is no independent determination of the density which might be very high, of the order that one would expect for the transition from e-h plasma to bound excitons. Thus many-body effects might be important.

The laser shows very interesting behaviour which might help to determine the origin of the second lasing mode. There is a switching between the two laser modes as the temperature or the pump power is changed. At low pump powers and low temperatures only the first laser line (L1) is present. There is a quite wide range of pump intensities and a very narrow range of temperatures for which the laser works in multimode in which

both modes are lasing. At high powers or high temperatures the second lasing line, L2, dominates. It has to be stressed that with increasing temperature the L1 line disappears, but with increasing pump power it saturates (when L2 turns on) and then slowly diminishes in absolute intensity (see Figures 3.1 and 3.2). The crossover as the temperature is changed in the experiment takes place within a very narrow interval of about 5K (Figure 3.3). With the onset of L2 an increase of up to 33 % in the slope can be measured as a kink in the response curve, in comparison with the gain saturation observed at lower temperatures where L2 is absent (see inset in Fig 3.3)

We need to find a model for a two-mode laser, which could explain such behaviour. In this chapter we assume that the second lasing mode is also associated with an exciton-like state, higher in energy than the ground state.

4.2 Model

The model we consider in this Chapter is schematically shown in Figure 4.1. Levels “0” and “3”, shown in the diagram 4.1, correspond to the valence and the conduction band of the semiconductor, respectively. Level “1” is a ground state exciton while level “2” is a higher excitonic state in the structure. Since excitons cannot be packed closer than around a Bohr radius the maximum occupancy of levels “1” and “2” is limited and given by excitonic density of states for both levels, respectively. We call these maximum occupancies N_1 for level “1” and N_2 for level “2”.

External excitations create free electrons and holes in the semiconductor. This corresponds to pumping the electrons from the valence (level “0”) to the conduction (level “3”) bands. Then they populate the two excitonic states, levels “1” and “2”, with rates $I_p^{(1)}$ and $I_p^{(2)}$, respectively. The first laser action (L1 line) takes place between level “1” and level “0”, while the second laser mode (L2 line) is between levels “2” and “0”.

There are also other transitions present in the system. Phonons and thermal photons would cause transitions between levels “2” and “1” since the energy difference between these levels is only 14 meV. We introduce γ_{21} and γ_{12} as emission and absorption rates, respectively, of thermal photons and η_{21} and η_{12} emission and absorption rates of phonons. Absorption and emission rates are connected through the Boltzmann factors

$$\gamma_{12} = \gamma_{21} e^{-\frac{\Delta}{kT}} \qquad \eta_{12} = \eta_{21} e^{-\frac{\Delta}{kT}}, \qquad (4.1)$$

where Δ is the energy difference between the two lasing modes. We also consider sponta-

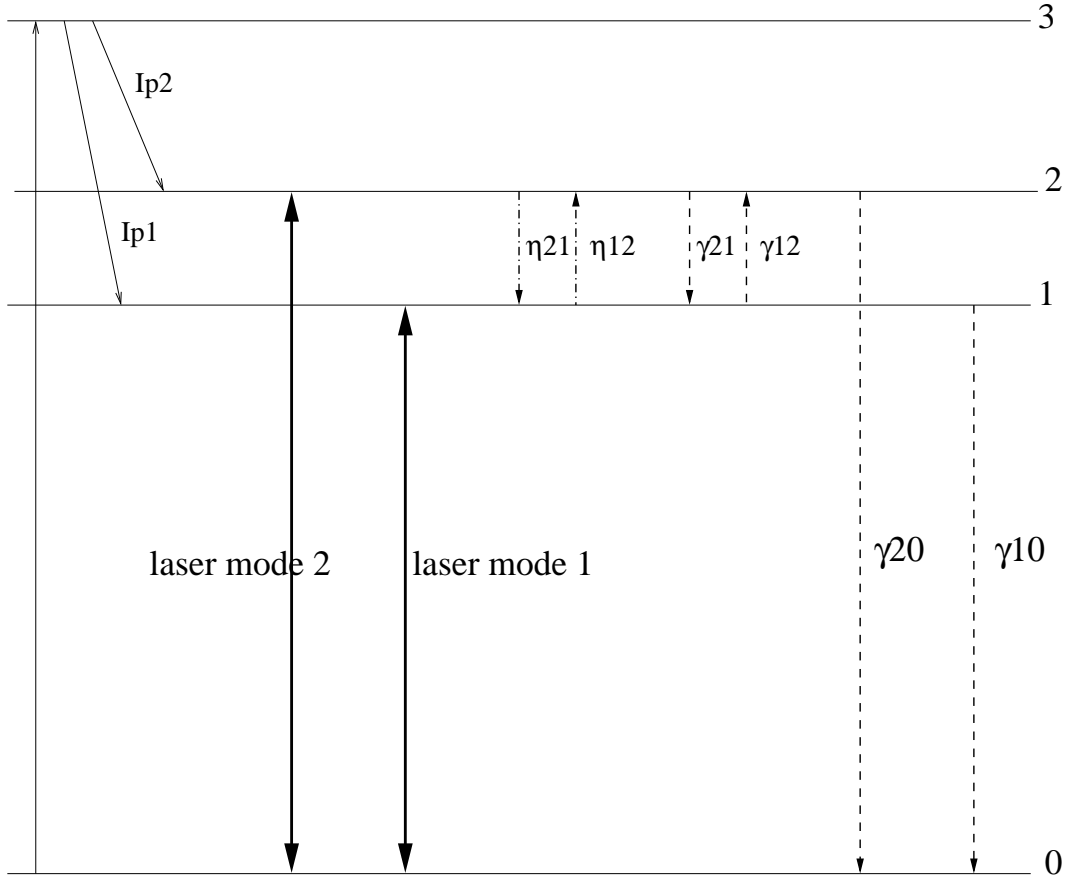


Figure 4.1: Sketch of the model for a two-mode laser system. Various levels and the transitions between them are shown. Bold solid lines correspond to laser actions, dashed lines correspond to photon spontaneous emission and absorption while dotted-dashed lines correspond to phonon emission and absorption.

neous emissions of photons to modes different from the two lasing modes for both lasing levels with rates γ_{20} and γ_{10} , respectively.

This model combines two standard rate equations models for the semiconductor laser and for the atomic laser. The levels “0” and “3” are alike in the semiconductor model where the maximum occupancy of the levels are not imposed while levels “1” and “2” are the same as in atomic lasers characterised by the parameters N_1 and N_2 which involve saturation of the levels.

Without detailed calculations we can see that raising the temperature thermally depopulates level “1” into level “2”. A strong pumping also increases the population of level “2”

over level “1”, provided the trapping from level “2” into level “1” is relatively inefficient in comparison to the rate of emission from level “2”, and provided also that the population of level “1” can saturate.

Introducing the abbreviation $r_{21} = \gamma_{21} + \eta_{21}$ and using equation (4.1) we obtain, from a detailed balance, the rate equation for the population of the higher excitonic state (level “2”), n_2

$$\begin{aligned} \frac{dn_2}{dt} = & Ip^{(2)}(N_2 - n_2) - r_{21}n_2(N_1 - n_1) + r_{21}e^{-\frac{\Delta}{kT}}n_1(N_2 - n_2) \\ & - \gamma_{20}n_2 - n_2(1 + S_2)g_2 + (N_2 - n_2)S_2g_2. \end{aligned} \quad (4.2)$$

The first term in equation (4.2) corresponds to the pumping of level “2” and is proportional to the pump power and the difference between the maximum number of excitons, N_2 , and the current number of excitons in this state, n_2 . The second term, which describes transitions from level “2” to level “1”, caused by phonons or thermal photons is proportional to the number of excitons in level “2” and to the difference between the maximum number of excitons in level “1”, N_1 , and the current number of excitons in this state, n_1 . Similarly the third term describes the transitions from level “1” to level “2”, caused by phonon or thermal photons. The fourth term corresponds to the spontaneous emission of photons to modes other than the lasing modes. Finally, the fifth term describes a stimulated emission of photons to the L2 lasing line and is proportional to the number of excitons in level “2”, n_2 , and to the factor $1+S_2$, where S_2 is a number of photons in the L2 mode. The sixth term gives the stimulated absorption of photons from the L2 lasing mode.

Similarly, the rate equation for the number of excitons in the ground state (level “1”), n_1 is

$$\begin{aligned} \frac{dn_1}{dt} = & Ip^{(1)}(N_1 - n_1) + r_{21}n_2(N_1 - n_1) - r_{21}e^{-\frac{\Delta}{kT}}n_1(N_2 - n_2) \\ & - \gamma_{10}n_1 - n_1(1 + S_1)g_1 + (N_1 - n_1)S_1g_1, \end{aligned} \quad (4.3)$$

where S_1 is the number of photons in the L1 lasing mode.

The rate equation for the photon number in the L1 mode is

$$\frac{dS_2}{dt} = -\kappa_2S_2 + (n_2 - (N_2 - n_2))S_2g_2, \quad (4.4)$$

while in the L2 mode is

$$\frac{dS_1}{dt} = -\kappa_1 S_1 + (n_1 - (N_1 - n_1))S_1 g_1, \quad (4.5)$$

where κ_1 and κ_2 are the cavity decay rates for the L1 and the L2 lasing mode, respectively.

4.3 Steady State Behaviour

We are now interested in a steady state behaviour of these four coupled equations (4.2) - (4.5). We need to consider four different regimes:

1. $S_1 > 0$ and $S_2 > 0$, both modes are lasing.
2. $S_1 > 0$ and $S_2 = 0$, 1st mode is lasing, 2nd is not lasing.
3. $S_1 = 0$ and $S_2 > 0$, 1st mode is not lasing, 2nd is lasing.
4. $S_1 = 0$ and $S_2 = 0$, both modes are not lasing.

Experimentally all four regimes were observed in the same structure for different temperatures and pump powers (see Chapter 3). It can be shown that, to have all four regimes in the same structure in our model, the laser parameters have to satisfy the following three conditions

$$A = \frac{N_1}{2} - \frac{\kappa_1}{2g_1} > 0 \quad (4.6)$$

$$C = \frac{N_2}{2} - \frac{\kappa_2}{2g_2} > 0 \quad (4.7)$$

$$\frac{N_2 g_2}{\kappa_2} > \frac{N_1 g_1}{\kappa_1}. \quad (4.8)$$

If we assume that the cavity decay rates for both laser modes are the same $\kappa_1 = \kappa_2$, the condition (4.8) means that the oscillator strength times the density of states for level “2” has to be larger than that of level “1”. It is very unlikely that the oscillator strength for any higher excitonic state would be larger than that of the ground state, but it is very probable that the density of states would be larger for the higher state and thus the condition would be satisfied.

In the Chapter 3 we argued that the second lasing line is connected with quasi-2D-

exciton-like states strongly perturbed by the quantum wire potential, resonant with (and thus decaying into) the continuum states of the wire. The density of such states would be much bigger than that of the ground state excitons (see Figure 3.5).

Let us now consider in more detail the four different regimes as the temperature and pump power are changed.

- Multimode operation of the laser: $S_1 > 0$ and $S_2 > 0$. Using equations (4.2) - (4.5) we can calculate the intensities of both laser lines in a steady state, assuming that both photon modes are occupied. Introducing abbreviations

$$B = \frac{N_1}{2} + \frac{\kappa_1}{2g_1}, \quad (4.9)$$

and

$$D = \frac{N_2}{2} + \frac{\kappa_2}{2g_2}, \quad (4.10)$$

the intensities of the modes will be

$$S_2 = \frac{r_{21}}{\kappa_2} (BCe^{-\frac{\Delta}{kT}} - AD + C \frac{Ip^{(2)}}{\gamma_{21}} - \frac{\gamma_{20} + g_2}{\gamma_{21}} D), \quad (4.11)$$

$$S_1 = \frac{r_{21}}{\kappa_1} (-BCe^{-\frac{\Delta}{kT}} + AD + A \frac{Ip^{(1)}}{\gamma_{21}} - \frac{\gamma_{10} + g_1}{\gamma_{21}} B). \quad (4.12)$$

Notice that the first two terms in equation (4.11), out of which only the first one is temperature dependent in the whole equation, have the same magnitude but opposite sign to the analogous terms in equation (4.12). These terms cause the competition between the two modes as the temperature is changed. At low temperatures the first two terms in equation (4.11) would be negative, and when the pumping (the third term) is too low to compensate them and the losses described by the fourth term, the L2 line will not be present. Similarly, from equation (4.12) we can see that at high temperatures the L1 line will not be present. As the temperature is changed, the rate equation model predicts the same switching of modes, as was experimentally observed (see Chapter 3).

- At low temperatures and pumping rates, when $S_1 > 0$ and $S_2 = 0$, the intensity of

the L1 lasing line will be

$$S_1 = \frac{A I p^{(1)} - B(\gamma_{10} + g_1)}{\kappa_1} + \frac{N_2}{\kappa_1} * \frac{A I p^{(2)} - B(\gamma_{20} + g_2) e^{-\frac{\Delta}{kT}}}{A + B e^{-\frac{\Delta}{kT}} + \frac{I p^{(2)}}{\gamma_{21}} + \frac{\gamma_{20} + g_2}{\gamma_{21}}} \quad (4.13)$$

- At high temperatures or pump powers, when $S_1 = 0$ and $S_2 > 0$, the intensity of the L2 line would be

$$\frac{1}{\kappa_2} * (C I p^{(2)} - (\gamma_{20} + g_2) D) + \frac{C I p^{(1)} e^{-\frac{\Delta}{kT}}}{C e^{-\frac{\Delta}{kT}} + D + \frac{I p^{(1)}}{\gamma_{21}} + \frac{\gamma_{10} + g_1}{\gamma_{21}}}. \quad (4.14)$$

Equations (4.11) - (4.14) have quite complicated forms, therefore it will be easier to study the behaviour of the system by plotting the results for particular parameters. We developed this model before the detailed calculations of spectra, described in Chapter 3, were obtained and thus not all values of input parameters were available. We noticed, however, that the qualitative behaviour of the system is not that sensitive to the input parameters, provided that the conditions (4.6) - (4.8) are satisfied. We choose the input parameters so that the temperature transition region is the same as in the experiment. For different, but yet realistic, parameters the qualitative behaviour would remain the same, but the transition temperature would change.

The most important parameter which determines the thermal coupling of the two modes is Δ . We use exactly the same value of 14 meV for Δ as in the experiment. The exact values of other parameters are very difficult to determine. In this work we use approximate values, but realistic ones for these types of structures. We normalise the parameters so that the gains $g_1 = g_2 = 1$, $N_2/N_1 = 100$, $\kappa_1/g = \kappa_2/g = 8.81$, $r_{21}/\gamma_{20} = r_{21}/\gamma_{10} = 10$. We choose $I_p^{(1)}$ to be 0, which is a physical assumption, because the exciton has to get into the well first before it can get into the wire.

In Figure 4.2 we present a phase diagram for our system. The four different phases are marked in Fig 4.2. The phase diagram recovers the experimental behaviour, shown in Figures 3.1 and 3.2. Let us first discuss the behaviour of the system at a fixed temperature, lower than 59K. At very low pump powers there is no lasing in the system. With the increase in the pump power the L1 laser mode appears first. When the pump power is increased further, the L2 laser action starts and the system lases in multimode. The intensity of the L1 line saturates when the L2 mode appears, while the intensity of the L2 increases with the pump power (see Figure 4.4). Thus the L1 line slowly diminishes

in absolute intensity in agreement with experiment (see Figure 3.1). At such high pump intensities, it is also possible that the temperature of the T-wire would rise above the nominal reservoir temperature, given on the graphs, which would additionally suppress the intensity of the L1 line.

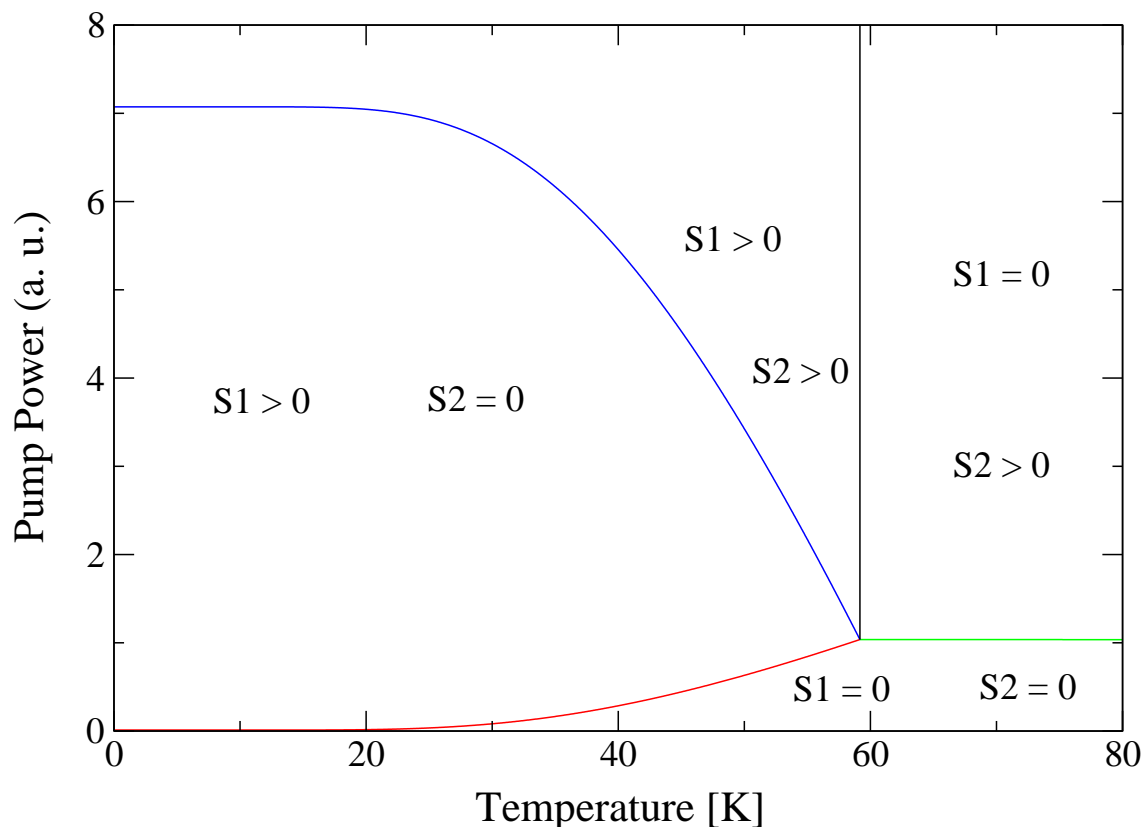


Figure 4.2: Phase diagram for a two-mode laser. Phase boundaries are shown as solid lines. The red (green) solid line corresponds to transition between the lack of lasing and the appearance of the L1 (L2) lasing mode. The blue line is a phase boundary between the presence of the L1 mode only and the multimode operation (presence of both L1 and L2 modes). The black line corresponds to the transition from simultaneous lasing of L1 and L2 modes and the presence of the L2 line only.

Similarly, when we fix the pump power at a value higher than the threshold for lasing and change the temperature, we recover the experimental behaviour, given in Figure 3.2. At low temperature the L1 mode is lasing, as the temperature is increased both L1 and L2 modes are present, and finally the L1 line disappears and only the L2 mode is present. This switching usually takes place within a narrow interval of temperatures (see Figure 4.3).

In the inset of Figure 4.3 we present the laser intensity versus pump power for three temperatures near the transition. With the onset of L2 an increase in the slope can be

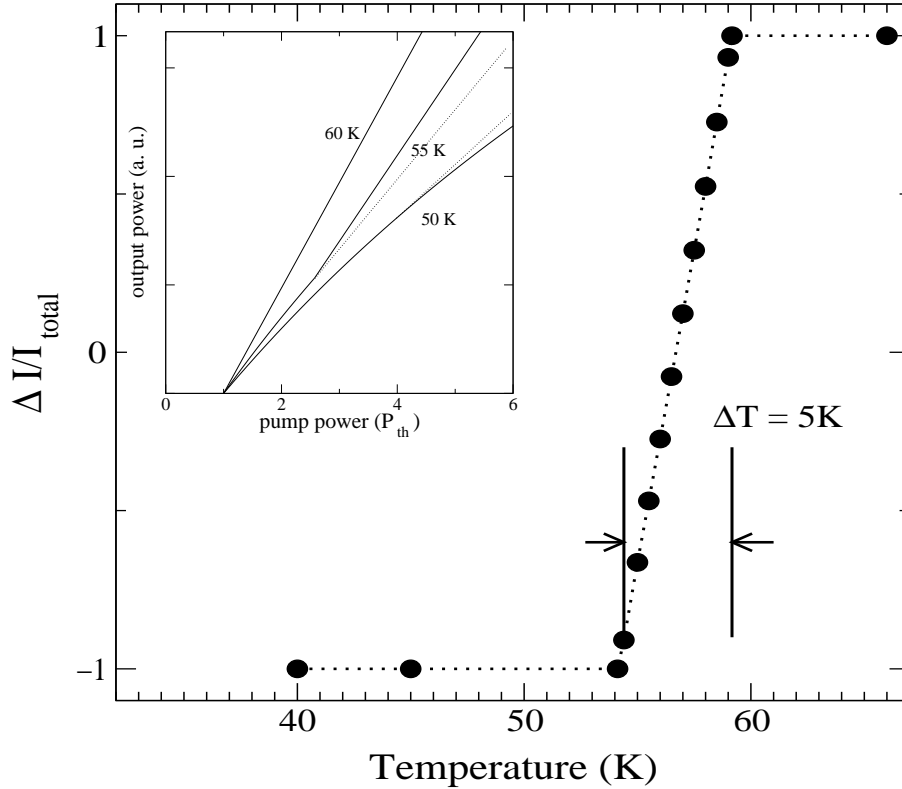


Figure 4.3: Calculated normalised difference of intensities $(I_{L2} - I_{L1})/I_{Total}$ as a function of temperature in the transition region. Inset: Laser intensity versus pump power for three temperatures near the transitions (the pump power is normalised to the threshold value at each temperature). The straight dotted lines are guides to the eye. This Figure should be compared to the experimental Figure 3.3

observed as a kink in the intensity curve, in comparison with the gain saturation observed at lower temperatures where L2 is absent in agreement with experiment (see inset in Fig 3.3 a). The intensity at 60 K comes from the L2 line while at 50 K from the L1 line only. At 55K both lasing lines contribute, as shown in Figure 4.4.

Figure 4.3 presents the normalised difference of the two mode intensities and shows that, in agreement with experiment (see Figure 3.3 a), switching takes place within a narrow interval. We choose parameters so that the switching takes place within an interval $\Delta T \approx 5\text{K}$ around 55K. For different, but still realistic, parameters the transition temperature would be different but the qualitative behaviour would remain the same. At temperatures

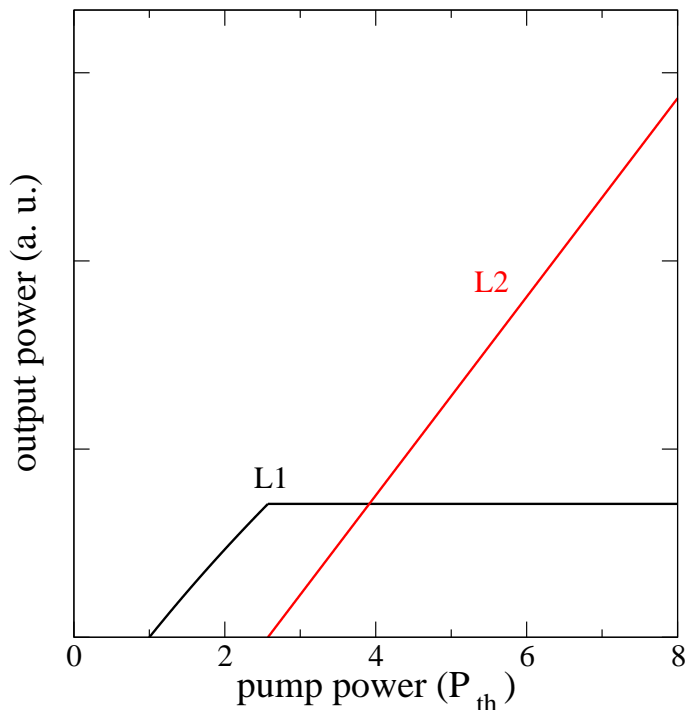


Figure 4.4: Intensity of the L1 (black curve) and the L2 (red curve) lasing modes at 55 K. When the L2 line appears the total intensity has a kink (see Figure 4.3).

above 55K the intensity of L2 increases monotonically with pump power, while L1 starts to diminish once both intensities become comparable.

4.4 Conclusion

We have shown, using a simple rate equation model, that the experimental results described in Chapter 3 can be explained assuming that the laser lines come from two different excitonic states in the structure. The most important qualitative features of the model that are necessary to explain the data are:

- the saturation of the states associated with the lasing lines,
- the temperature-dependence of the thermal occupation of these states,
- a relatively inefficient trapping from the higher to the lower lasing state in comparison to the rate of photon emission from the higher lasing state.

Using this model we have recovered:

- the switching between the two modes as temperature is changed,
- the saturation of the L1 line as the pump power is increased,
- the region of a multimode operation,
- experimentally observed behaviour of intensities of the two lasing lines.

This very good qualitative agreement between the model and the experiment suggests that we indeed have lasing from two different excitonic states in the structure. Motivated by this agreement we performed detailed calculations, presented in the Chapter 3, to identify the L2 excitonic state.

Chapter 5

Summary and Future Directions

5.1 Summary

In this work we have developed a method to calculate electron-hole states in quantum wires. We have included the single-particle potential and the Coulomb interaction between the electron and hole on an equal footing, and have performed exact diagonalisation of the two-particle problem within a finite basis set. We have calculated energies, oscillator strengths for radiative recombination, and two-particle wave functions for the ground state exciton and around 100 excited states in a T-shaped wire.

We have studied in detail the shape of the wave functions to gain insight into the nature of the various states for selected symmetric and asymmetric wires in which laser emission has been experimentally observed. We have found

- That the first group of excited states shows an *s*-like excitonic character where the electron is localised in the wire but is bound to the hole which spreads into one of the wells. Due to the fact that the electron and hole are not localised in the same region, we have a group of low oscillator-strength states just above the ground state.
- That the group of low oscillator-strength states is followed by a number of states with large oscillator strength which are 2D excitonic states scattered on the T-shaped intersection.

We have also performed a detailed study of the exciton binding and confinement energies as a function of the well width and Al molar fraction for symmetric and asymmetric wires. We have shown

- That the highest binding energy in any structure so far constructed is calculated to be 16.5 meV which is much smaller than previously thought.
- That for optimised asymmetric wires, the confinement energy is enhanced but the binding energy is slightly lower with respect to those in symmetric wires.
- That for GaAs/Al_xGa_{1-x}As wires we have obtained an upper limit for the binding energy of around 25 meV in a 10 Å wide GaAs/AlAs structure which suggests that other materials need to be explored in order to achieve room temperature applications. In_yGa_{1-y}As/Al_xGa_{1-x}As might be a good candidate.

Our calculations are being used to design improved excitonic lasers which will operate at room temperature. In particular we have studied in detail the GaAs/Al_xGa_{1-x}As structures in order to optimise the confinement energy of the wire.

We have described an experimental observation of an interesting phenomenon of a two-mode lasing in asymmetric T-shaped wires. We have then

- Developed a rate equation model for a two-mode laser. Assuming that the laser action takes place for two different exciton-like states, we can reproduce the same qualitative behaviour of the laser, as observed in the experiment.
- Applied the detailed numerical calculations for structures used in this experiment and identified the origin of the two laser modes. The first lasing line comes from the ground state exciton while the second line is most probably associated with quasi-2D-exciton-like states strongly perturbed by the quantum wire potential

5.2 Future Directions

- Our calculations are being used to design quantum wire lasers which would operate at room temperature. This work, in collaboration with Bell-Laboratories, is still in progress and detailed calculations for structures with different materials or shapes might be useful.
- It would be of interest to perform the rate equation calculations for the exact parameters of the structures used in the experiment.
- More complex extensions could consider doped quantum wires or including a finite concentration of electron-hole pairs in the wire.

Appendix A

Convergence of the T-shaped Wire Calculations

Table A.1: Convergence of the energy (E) in meV and the oscillator strength (OS) for states: 1st, 2nd, and 25th in the symmetric 70 Å quantum wire (as marked in Fig. 2.2, 2.3 and 2.4) with respect to the size of the basis set used in diagonalisation.

Number of Basis Functions	1st		2nd		25th	
	E	OS	E	OS	E	OS
10 x 10 x 10	41.79	2.96	48.72	0.98		
15 x 15 x 15	41.44	3.66	48.55	1.25	63.34	2.42
17 x 17 x 17	41.41	3.75	48.54	1.28	63.32	2.50
20 x 20 x 20	41.36	3.92	48.51	1.36	63.29	2.62
21 x 21 x 21	41.34	3.99	48.51	1.38	63.28	2.66

Table A.2: Convergence of the energy (E) in meV and the oscillator strength (OS) for states: 1st, 2nd, and 25th in the symmetric 70 Å quantum wire (as marked in Fig. 2.2, 2.3 and 2.4) with respect to the number of points on the 2D grid.

Number of Points	1st		2nd		25th	
	E	OS	E	OS	E	OS
119 x 119	41.44	3.66	48.55	1.25	63.34	2.42
203 x 203	41.62	3.57	48.71	1.23	63.54	2.31
245 x 245	41.61	3.66	48.73	1.24	63.55	2.35

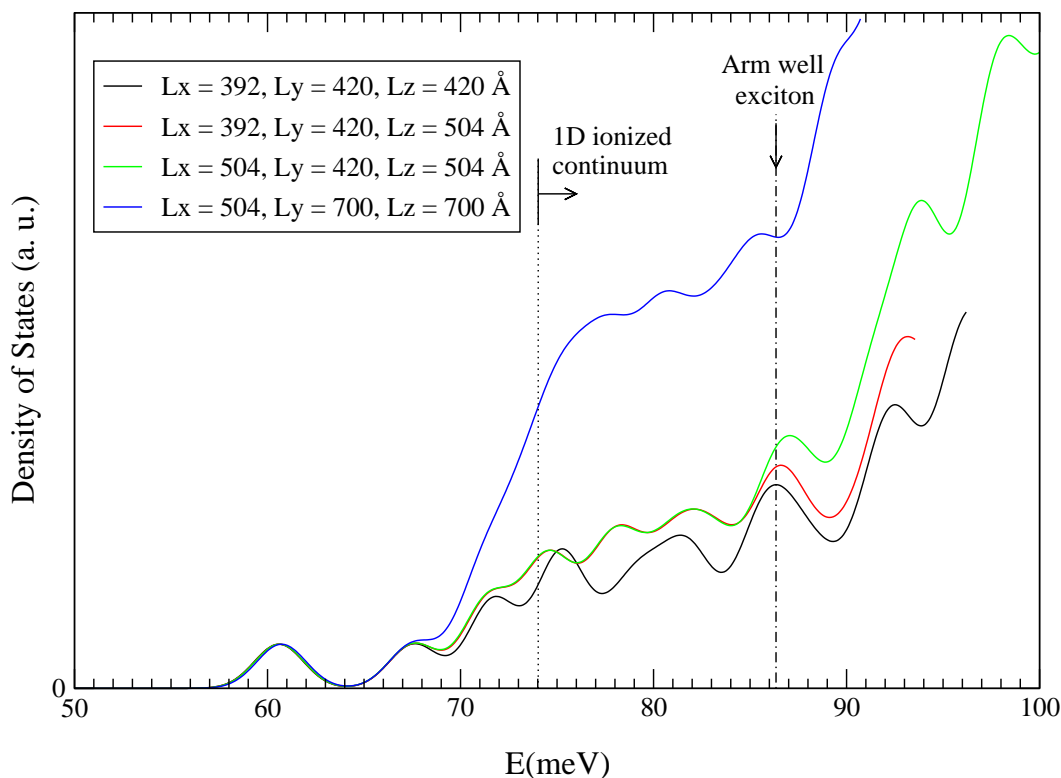


Figure A.1: Density of states in an asymmetric T-shaped structure with $D_x = 56$ Å, $D_y = 140$ Å discussed in Chapter 3 (Fig. 3.5) for four different unit cells. The line is produced by a Gaussian broadening with 1.5 meV HWHM of calculated discrete energies. Because our system is finite we obtain only a sampling of the continuum states. When we increase the unit cell size we automatically calculate more states within the same energy region thus the density of states, for energies above the onset of continuum states, grows. However, the features of the curves remain the same, suggesting that the energies are well converged with respect to the unit cell size.

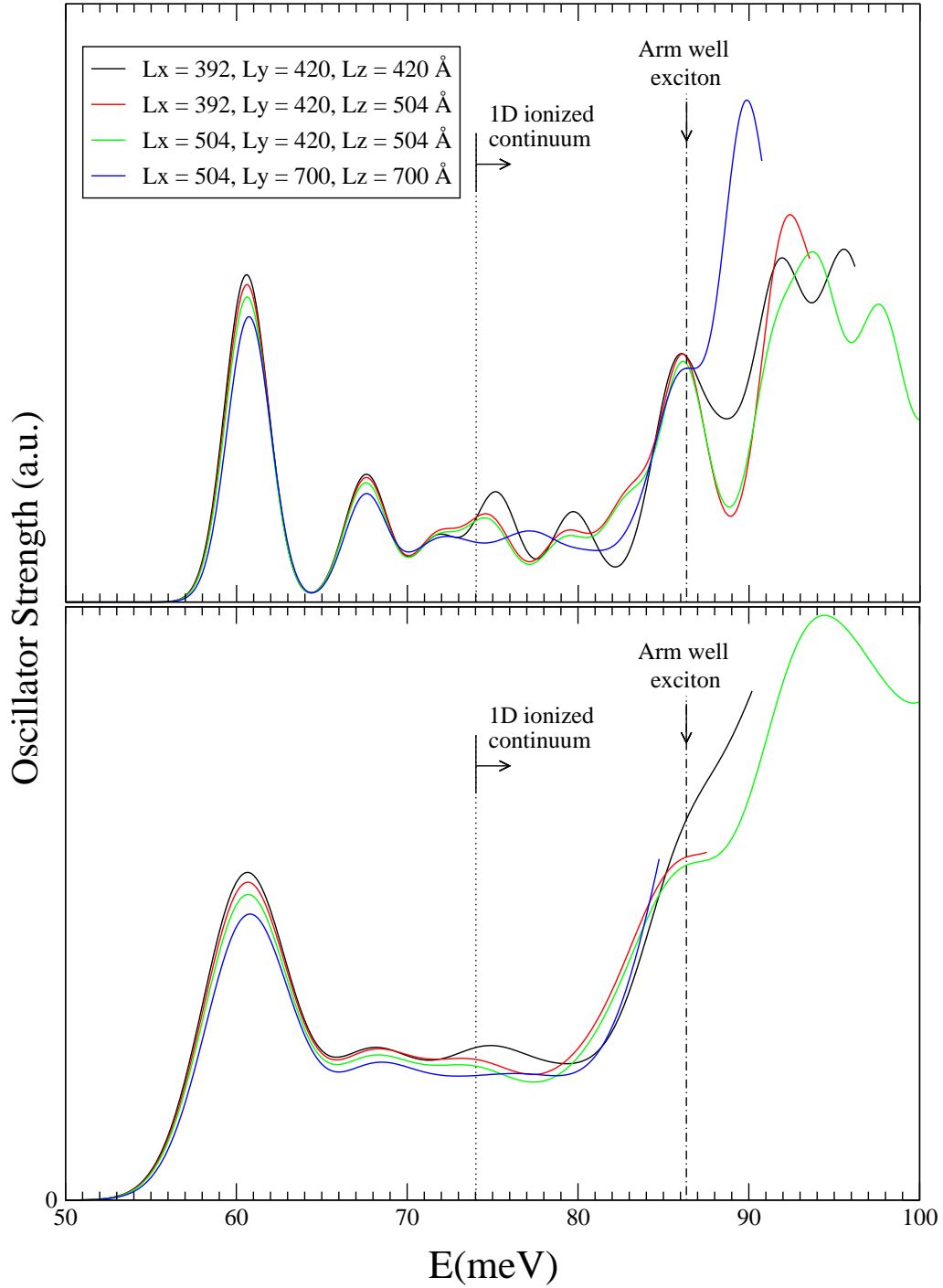


Figure A.2: Oscillator strength versus energy in an asymmetric T-shaped structure with $D_x = 56 \text{ \AA}$, $D_y = 140 \text{ \AA}$, discussed in Chapter 3 (Fig. 3.5), for four different unit cells. The line is produced by a Gaussian broadening with 1.5 meV (upper panel) and 3 meV (lower panel) HWHM of calculated discrete states.

Appendix B

Comments on the Effective Mass Approximation

Calculations of the T-shaped wire states are performed using the effective mass approximation with an anisotropic hole mass. In the effective mass approximation electron and heavy hole single parabolic bands are assumed. This approximation is justified in the energy region of interest.

In Figure B.1 (upper panel) we present the hole band structure along the wire direction, taken from [23], for sample S2 (see Table 2.1) experimentally studied in [3], which consist of 53 Å Stem and 48 Å Arm quantum wells with AlAs barriers. For the same sample, in Figure B.1 (lower panel), we present the contribution from different k_z states in a ground and a first excited state wavefunction given by equation (2.2). $\sum_{i,j} |c_{i,j,k_z}|^2$ is plotted as a function of k_z . Notice, that the hole bands are parabolic for k_z up to around 0.013 Å⁻¹. The contribution from k_z higher than 0.013 Å⁻¹ is negligible for presented first two states. The higher states are more spatially extended than the first two states and thus they will decay in the k_z space even faster than the presented two states. The conduction band is shown to be parabolic for k_z up to 0.04 Å⁻¹ for AlAs barriers [24]. For lower Al concentration the conduction band is parabolic even for higher k_z up to 0.11 Å⁻¹ for Al concentration, $x=0.3$, while the spatial extension of states would be larger, and thus the region in k -space smaller than in the AlAs case. Thus the parabolic band effective mass approximation is justified for all structures being considered in this work.

Another issue is that the second hole band in Figure B.1 (upper panel), although parabolic in the energy region of interest, splits into two branches with different, by around factor of two, effective masses. The binding energies are, however, not that sensitive to the

hole effective mass. The binding energy of the light hole exciton with the hole mass around eight times smaller than the heavy hole mass differs only by 4 meV from the binding energy of the heavy hole exciton. Pfeiffer *et al* have shown that the electron and hole confinement energies calculated using the full eight band $\vec{k} \cdot \vec{p}$ method agree within about 1 meV with those obtained using the one band effective mass approximation [15]. In the presence of the Coulomb interactions the effect on the binding energy will be even smaller than that. Notice, that the binding energy in these structures is a function of the confinement energy (Fig. 2.7) with the changes in the confinement energy corresponding to on average six times smaller changes in the binding energy. Thus the difference in energies between the full eight band $\vec{k} \cdot \vec{p}$ methods and our calculations would be smaller than 1 meV for structures studied in this work.

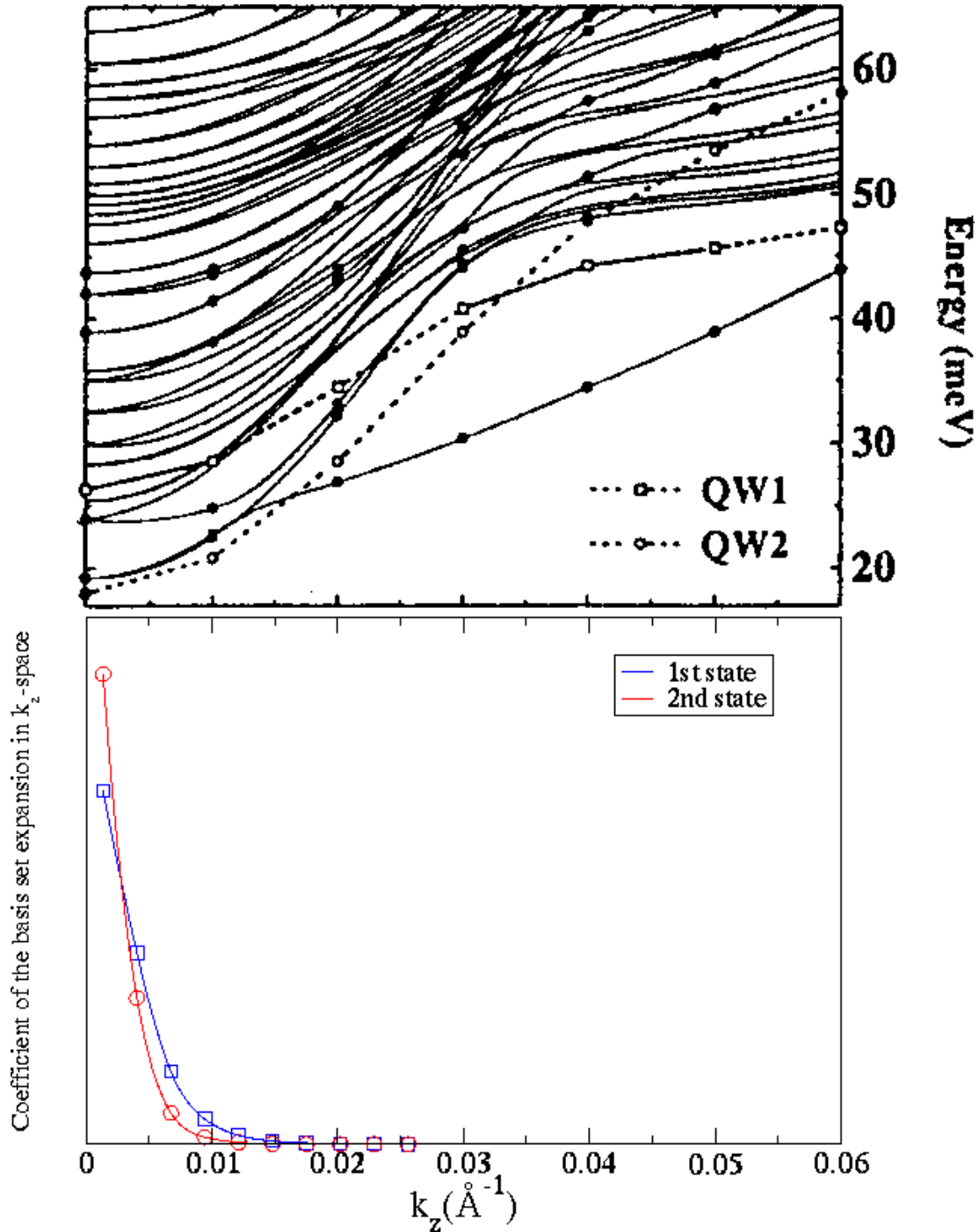


Figure B.1: Upper panel: Hole band structure along the z axis of the T-QWR. The full circles identify the states that are quasi-one-dimensional wire-like states or resonances. Dashed lines show the lowest-hole subbands of the isolated Arm and Stem quantum wells. Taken from [23]. Lower panel: Coefficient of the basis set expansion in k -space as a function of k in the z direction in the present calculations using the effective mass approximation.

Bibliography

- [1] Y. C. Chang, L. L. Chang, and L. Esaki, *Appl. Phys. Lett.* **47**, 1324 (1985).
- [2] H. Akiyama, T. Someya, M. Yoshita, T. Sasaki, and H. Sakaki, *Phys. Rev. B* **57**, 3765 (1998).
- [3] T. Someya, H. Akiyama, and H. Sakaki, *Phys. Rev. Lett.* **76**, 2965 (1996).
- [4] H. Gislason, W. Langbein, and J. M. Hvam, *Superlattices and Microstruct.* **22**, 217 (1997).
- [5] W. Langbein, H. Gislason, and J. M. Hvam, *Phys. Rev. B* **54**, 14595 (1996).
- [6] W. Wegscheider, L. N. Pfeiffer, M. M. Dignam, A. Pinczuk, K. W. West, S. L. McCall, and R. Hull, *Phys. Rev. Lett.* **71**, 4071 (1993).
- [7] J. Hasen, L. N. Pfeiffer, A. Pinczuk, S. He, K. W. West, and Brian S. Dennis, *Nature* **390**, 54 (1997).
- [8] J. Rubio, L. N. Pfeiffer, M. H. Szymanska, A. Pinczuk, S. He, H. U. Baranger, P. B. Littlewood, K. W. West, and B. S. Dennis, unpublished.
- [9] J. Rubio, L. N. Pfeiffer, M. H. Szymanska, A. Pinczuk, S. He, H. U. Baranger, P. B. Littlewood, K. W. West, and B. S. Dennis, unpublished.
- [10] S. Glutsch, F. Bechstedt, W. Wegscheider, and G. Schedelbeck, *Phys. Rev. B* **56**, 4108 (1997).
- [11] F. Rossi, G. Goldoni, and E. Molinari, *Phys. Rev. Lett.* **78**, 3527 (1997).
- [12] D. Brinkman and G. Fishman, *Phys. Rev. B* **56**, 15211 (1997).

- [13] G. W. Bryant, P. S. Julienne, and Y. B. Band, *Superlattices and Microstruct.* **20**(4), 601 (1996).
- [14] A. A. Kiselev and U. Rossler, *Semicond. Sci. Technol.* **11**, 203 (1996).
- [15] L. Pfeiffer, H. Baranger, D. Gershoni, K. Smith, and W Wegscheider, in K. Eberl et al. (eds.), *Low Dimensional Structures prepared by Epitaxial Growth or Regrowth on Patterned Substrates*, 93-100, 1995 Kluwer Academic Publishers.
- [16] M. C. Payne, M. P. Teter, D. C. Allan, T. A. Arias, and J. D. Joannopoulos, *Reviews of Modern Physics* **64**, 1045 (1992).
- [17] T. Kato, *Communications on Pure and Applied Mathematics* **10**, 151 (1957).
- [18] H. Akiyama, private communications
- [19] G. A. Narvaez., et al. *Physica E* **2**, 983 (1998).
- [20] G. S. Agarwal and S. Dattagupte *Phys. Rev. A* **26**, 880-887 (1982).
- [21] M. H. Szymanska, P. B. Littlewood, and R. J. Needs, *Phys. Rev. B* **63**, 205317 (2001).
- [22] L. Pfeiffer, private communications
- [23] G. Goldoni, F. Rossi, E. Molinari, A. Fasolino, *Phys. Rev. B* **55**, 7110 (1997).
- [24] S. Pescetelli, A. Di Carlo, and P. Lugli, *Phys. Rev. B* **56**, R1668 (1997).